Petroleum Science 20 (2023) 424–446

Contents lists available at ScienceDirect

Petroleum Science

journal homepage: www.keaipublishing.com/en/journals/petroleum-science

Original Paper

High-precision nonisothermal transient wellbore drift flow model suitable for the full flow pattern domain and full dip range

Wen-Qiang Lou [a, b, c], Da-Lin Sun [a], Xiao-Hui Sun [d], Peng-Fei Li [a], Ya-Xin Liu [e], Li-Chen Guan [a], Bao-Jiang Sun [a], Zhi-Yuan Wang [a, *]

[a] Offshore Petroleum Engineering Research Center, School of Petroleum Engineering, China University of Petroleum (East China), Qingdao, 266580, Shandong, China
[b] School of Petroleum Engineering, Yangtze University, Wuhan, 430199, Hubei, China
[c] Hubei Key Laboratory of Oil and Gas Drilling and Production Engineering (Yangtze University), Wuhan, 430199, Hubei, China
[d] College of Computer Science and Technology, China University of Petroleum (East China), Qingdao, 266580, Shandong, China
[e] Department of Petroleum Engineering, University of Tulsa, Tulsa, United States

ARTICLE INFO

Article history:
Received 28 November 2021
Received in revised form
10 November 2022
Accepted 14 November 2022
Available online 19 November 2022

Edited by Yan-Hua Sun

Keywords:
Drift closure relation
Non-isothermal model
High-precision
Multiphase flow solver
Wellbore pressure control

ABSTRACT

A reliable multiphase flow simulator is an important tool to improve wellbore integrity and production decision-making. To develop a multiphase flow model with high adaptability and high accuracy, we first build a multiphase flow database with 3561 groups of data and developed a drift closure relationship with stable continuity and high adaptability. Second, a high-order numerical scheme with strong fault capture ability is constructed by effectively combining MUSCL technology, van Albada slope limiter and AUSMV numerical scheme. Finally, the energy equation is coupled into the AUSMV numerical scheme of the drift flow model in the form of finite difference. A transient non-isothermal wellbore multiphase flow model with wide applicability is formed by integrating the three technologies, and the effects of various factors on the calculation accuracy are studied. The accuracy of the simulator is verified by comparing the measurement results with the blowout experiment of a full-scale experimental well.

1. Introduction

With the increasing demand for oil and gas resources, the exploration and development of oil and gas has gradually expanded to deep water and unconventional shale oil and gas fields. The complex working conditions brought by this situation include downhole high temperature and high pressure, complex well structures such as extended reach wells/horizontal wells, narrow safe operation windows, etc. These complex working conditions increase the probability of kick and lost circulation accidents and the difficulty of wellbore pressure control (Sun et al., 2018; Zhang et al., 2020). The multiphase flow analysis of formation fluid after invading the wellbore has become key to inverting the change law of wellbore pressure and formulating the well-killing scheme. The failure to accurately analyze the flow process in the wellbore will increase the risk of on-site construction and may lead to more serious blowouts (Sutton, 2013). Therefore, an accurate wellbore multiphase flow simulator is needed to improve our understanding of the kick evolution law, help drilling and completion engineers make correct decisions in field operation and improve operation safety.

The wellbore multiphase flow simulator with high accuracy depends on three aspects of model stability: one is the multiphase flow numerical algorithm with strong robustness and stability; another is the gas–liquid two-phase auxiliary relationship with strong continuity and a wide application range, and the third is the two-phase flow energy equation highly coupled with the multiphase flow control equation. For the simulation of multiphase flow in wellbores, scholars have proposed a variety of theoretical models. The drift flux model considers the slip effect between fluid phases and can be used to simulate the multiphase flow state with strongly coupled interphase motion (Ishii, 1977; Shi et al., 2005). The drift flow model is composed of a continuity equation and a mixed momentum equation of each phase. Because of its simple

* Corresponding author.
E-mail address: wangzy1209@126.com (Z.-Y. Wang).

https://doi.org/10.1016/j.petsci.2022.11.011

Nomenclature

A	Annular cross-sectional area, m^2
A', B'	Thermal resistance coefficient, (m k)/W
A_t	Cross sectional area of drill pipe, m^2
A_μ, B_μ, C_μ, D_μ	Drilling fluid characteristic constants
C_0	Distribution coefficient
c_g	Sound velocity in gas phase, m/s
c_l	Sound velocity in liquid phase, m/s
c_m	Sound velocity in gas–liquid two-phase flow, m/s
E_g	Gas volume fraction
e_g	Internal energy of gas, J/kg
E_l	Liquid holdup
e_l	Internal energy of liquid, J/kg
f	Friction coefficient
g	Gravitational acceleration, m/s^2
h_e	Gas enthalpy under formation conditions, J/kg
h_g	Enthalpy of gas, J/kg
h_l	Enthalpy of liquid, J/kg
k_e	Formation thermal conductivity, W/(m k)
L_p	Length of pipe, m
$N_{Eö}$	Eötvös numbers
p	Pressure, Pa
p_0	Ground pressure, Pa
Q_{flux}	Enthalpy of gas inflow, J/(m/s)
Q_{fric}	Friction heat, J/(m/s)
Q_{in}	Heat exchange rate between wellbore and surrounding environment, J/(m/s)
r_{co}	Casing outer diameter, m
r_{ti}	Drill pipe inner diameter, m
t	Time, s
T	Temperature in the annulus, °C
T_0	Ground temperature, °C
T_{sr}	Ambient temperature, °C
T_t	Temperature in drill pipe, °C
U_a	Heat transfer coefficient between annulus fluid and formation, W/(m^2 K)
U_t	Heat transfer coefficient between drill pipe fluid and annulus, W/(m^2 K)
v_g	Gas velocity, m/s
v_{gm}	Drift velocity, m/s
v_l	Liquid velocity, m/s
x	Spatial node, m
α	Included angle between pipe and horizontal direction, degree
θ	Well deviation angle, degree
μ_l	Liquid viscosity, mPa s
μ_w	Viscosity of water, mPa s
ρ_g	Gas density, kg/m^3
ρ_l	Liquid density, kg/m^3

and clear mathematical structure, it is superior to two fluid models in continuity, differentiability and computational efficiency. It is widely used in multiphase flow simulation in the field of petroleum engineering (Shi et al., 2005). The drift flow model has the characteristics of a hyperbolic equation and can explain all situations of gas–liquid two-phase flow in the pipeline (Han and Guo, 2015). To solve the drift flow model with hyperbolic characteristics, scholars have carried out in-depth research on finite differences and finite volumes. The semi-implicit four-point difference scheme based on pressure assumption correction (Nickens, 1987) is a representative finite difference scheme and is widely used in wellbore multiphase flow simulations. However, due to the poor conservation of the finite difference algorithm, it easily diverges in the iterative calculation process. The numerical scheme based on finite volume has high conservation characteristics and has become the mainstream method in multiphase flow simulation. For the discontinuous capture problem in two-phase flow, two typical schemes have emerged: flux vector splitting (FVS) and the flux difference scheme (FDS). Among them, FDS solves the multiphase flow control equations by numerical analysis, quasi linearizes the nonlinear equations by the chain rule and reconstructs an approximate linear coefficient matrix to solve the equations. It has high-precision discontinuous capture ability. The representative formats are the Roe scheme (Roe, 1981) and the Osher scheme (Osher and Solomon, 1982). By reconstructing the convective flux, FVS makes the equation closer to the physical characteristics, maintains the original format of the equation and has high solution efficiency but causes the problem of high numerical dissipation. The representative formats are the Steger and Warming scheme (Steger and Warming, 1981) and the van Leer scheme (van Leer, 1979). Liou and Stenfen combined the advantages of FDS and FVS formats to construct AUSM formats with high discontinuity capture ability and high computational stability (Liou and Steffen, 1993) and continuously updated and developed them in the follow-up to form AUSM-family formats (Liou, 1996, 2006). Evje and Fjelde (2002) and Evje and Flåtten (2003) constructed AUSM, AUSMV and AUSMD schemes for multiphase flow simulation based on the characteristics of the drift flow model, which plays an important role in promoting the numerical solution of the drift flow model. At present, transforming this kind of algorithm into an algorithm suitable for wellbore multiphase flow has become a research hotspot.

Based on the research basis of Evje and Fjelde, many researchers use AUSM numerical schemes to solve the drift flow model (Fjelde et al., 2016; Udegbunam et al., 2015; Eghorieta et al., 2018; Xu et al., 2018; Wang et al., 2020), but the gas is simplified and simulated by the ideal gas equation of state. In the actual drilling and production process, due to the great influence of temperature and pressure on the state of gas, the AUSM algorithm based on the ideal gas state equation cannot accurately predict the evolution law of wellbore pressure (Udegbunam et al., 2015). The coupling solution of a simple temperature field and multiphase flow equation is applicable to working conditions with small gas influx. When serious blowout occurs in the wellbore, the expansion work of gas in the whole wellbore will have a great impact on the fluid temperature in the wellbore. At this time, it is necessary to couple the energy equation of two-phase flow with the drift flow model (Sun et al., 2018).

The core auxiliary equation of the drift flow model is the drift closure relationship, which determines the application scope and prediction accuracy of multiphase flow simulation. At present, the closure relationship of drift flow model is divided into three types: (1) The mechanism model based on the physical characteristics of flow pattern in wellbore (Ansari et al., 1994; Hasan and Kabir, 2007; Hibiki and Ishii, 2005) has high accuracy, and there is a discontinuous problem at the boundary of flow pattern transformation, resulting in difficulty in solving the convergence of multiphase flow equation. (2) The discontinuity of the flow pattern transformation boundary is optimized by introducing a smoothing function or a weighting function (Shi et al., 2005; Tang et al., 2019), which solves the problem that it is difficult to converge on the solution of the multiphase flow equation but increases the difficulty of calculation and reduces the accuracy of the original relationship. (3) Another

idea is not to develop an independent closed relation based on flow pattern recognition (Choi et al., 2012; Bhagwat and Ghajar, 2014; Wang et al., 2017; Liu et al., 2020; Lou et al., 2022). The model has good numerical stability and low calculation cost. The accuracy and scope of application of this closed relation depend on the information coverage of experimental data and the number of factors covered by the equation. Among them, the drift closure relationship not based on flow pattern division has good continuity, which is highly promoted in the solution of the drift flow model. At the same time, it has been widely studied by scholars. Improving the application scope and prediction accuracy of the drift closure relationship has become an important topic in multiphase flow simulation.

In summary, we summarized the key influencing factors for the development of a high-precision wellbore multiphase flow simulator. Based on the analysis and optimization ideas of the three factors in Fig. 1, we carried out research. The structure of this paper is as follows: in Section 2, we give the control equation and auxiliary equation of the wellbore multiphase flow model. Based on the multiphase flow experimental database, we develop a drift closure relationship suitable for the full dip range in the full flow regime domain. In Section 3, we present the coupled solution scheme of the drift flow model and energy equation and improve the accuracy of the algorithm. In Section 4, we verify the prediction effect of the drift closure relationship, analyze the factors affecting the simulation accuracy of multiphase flow and verify the nonisothermal transient multiphase flow algorithm by using the experimental data of full-scale test wells.

2. Model formulation

As shown in Fig. 2, the gas–liquid two-phase flow in the wellbore during drilling or well-killing is a multifactor interactive process involving factors such as wellbore size, well structure, fluid physical parameters, formation temperature field and reservoir coupling (Sun et al., 2018). To reveal the evolution law of key parameters such as flow velocity, porosity, pressure and temperature in the process of gas–liquid two-phase flow in wellbores, it is necessary to construct the transient wellbore multiphase flow control equation. To derive the governing equation of wellbore multiphase flow, we make the following assumptions:

(1) Considering that the flow is one-dimensional, the fluid in the wellbore is compressible.
(2) Considering radial heat transfer of wellbore.
(3) The changes in the thermophysical properties of the drill pipe, casing, cement and formation (such as specific heat capacity and thermal conductivity) are ignored.
(4) Ignoring the mass transfer between gas and liquid.
(5) Considering rock cuttings as the constituent phase of drilling fluid.

2.1. Governing equation of gas–liquid two-phase flow

2.1.1. Continuity and momentum equations

Many theoretical models have been proposed for multiphase flow simulation in wellbores. The drift flow model is widely used because of its simple and clear mathematical structure and good multiphase flow calculation effect. The three transport equations of the drift flow model are composed of two mass conservation equations and a mixed momentum equation. The coupling between phase velocity fields is determined by the drift relationship of gas and liquid. According to the coupling characteristics between the wellbore and formation in the whole well section, continuity equations of gas production and non-gas production intervals are established (Wang et al., 2016).

The continuity equations of the drilling fluid phase and gas phase are given by Eqs. (1) and (2), respectively. For the non-production interval, $q_g = 0$, for the production interval, $q_g \neq 0$.

$$\frac{\partial(AE_l\rho_l)}{\partial t} + \frac{\partial(AE_l\rho_l v_l)}{\partial x} = 0 \tag{1}$$

$$\frac{\partial(AE_g\rho_g)}{\partial t} + \frac{\partial(AE_g\rho_g v_g)}{\partial x} = q_g \tag{2}$$

Mixed momentum equation in wellbore:

$$\frac{\partial(AE_g\rho_g v_g + AE_l\rho_l v_l)}{\partial t} + \frac{\partial\left(AE_g\rho_g v_g^2 + AE_l\rho_l v_l^2 + Ap\right)}{\partial x} = -AF_w - A\rho_m g\cos\theta \tag{3}$$

2.1.2. Energy conservation equations

The physical parameters of the gas–liquid phase in multiphase flow Eqs. (1)–(3) are all functions of temperature. These variables will have an internal impact on the pressure and temperature in wellbore flow at the same time. The impact of temperature on multiphase flow in high-temperature and high-pressure ultradeep wells cannot be ignored. Therefore, it is necessary to establish a wellbore transient temperature field model to solve the multiphase flow process. Considering the heat exchange between the wellbore and surrounding formation, flow coupling of the wellbore reservoir, flow friction heat generation and Joule Thomson effect of gas, the energy conservation equation of wellbore multiphase flow is obtained (Sun et al., 2018).

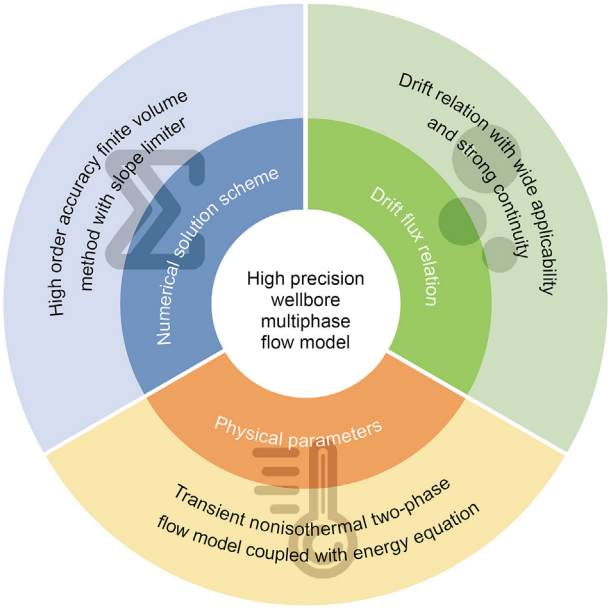

Fig. 1. Schematic diagram of key influencing factors and optimization ideas of wellbore multiphase flow model.

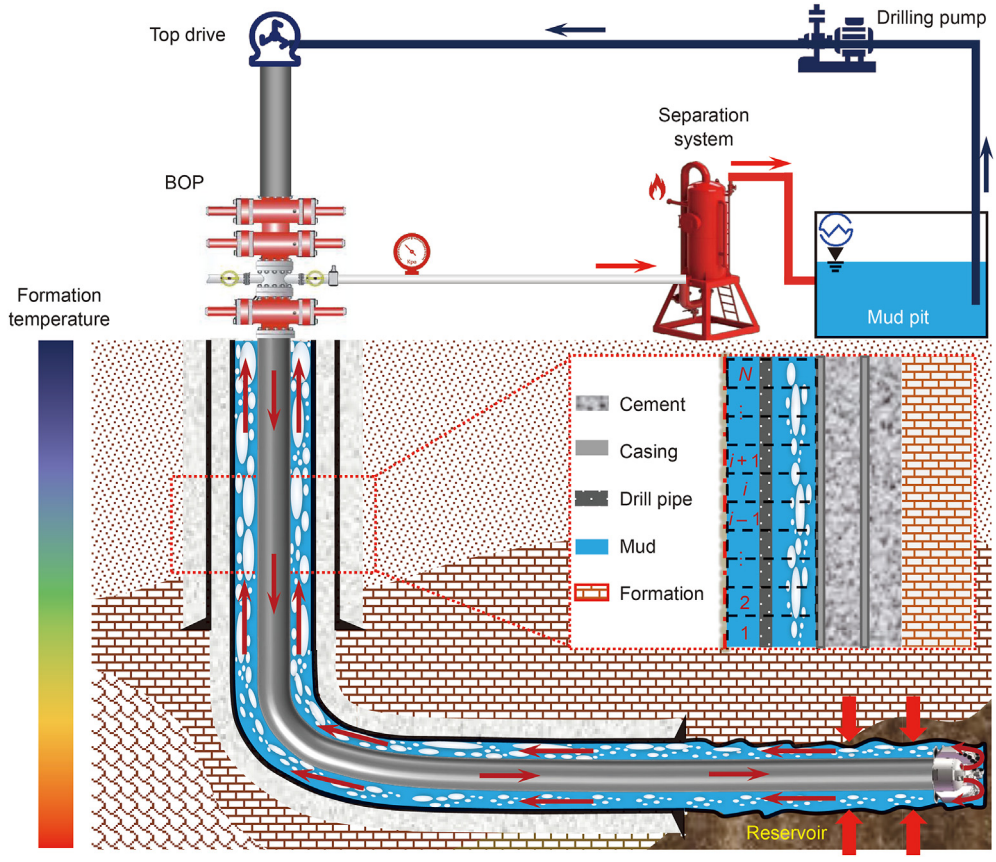

Fig. 2. Schematic diagram of multiphase flow after well kick.

$$\frac{\partial}{\partial t}\left[AE_g\rho_g\left(e_g+v_g^2/2\right)+AE_l\rho_l\left(e_l+v_l^2/2\right)\right]+\frac{\partial}{\partial x}\left[AE_g\rho_g v_g\left(h_g+v_g^2/2\right)+AE_l\rho_l v_l\left(h_l+v_l^2/2\right)\right]=-A\left(E_g\rho_g v_g+E_l\rho_l v_l\right)g\cos\theta+Q_{in}+Q_{fric}+Q_{flux} \tag{4}$$

The enthalpy and internal energy in the process of wellbore multiphase flow are functions of temperature and pressure. According to the thermophysical properties of fluid, the relationship between enthalpy and internal energy is (Liao et al., 2019):

$$dh_i=de_i+d(p/\rho_i)=C_i dT+d(p/\rho_i)\quad(i=l,\ g) \tag{5}$$

By substituting continuity Eqs. (1), (2) and (5) into Eq. (4), the left term of the energy equation can be transformed into:

$$A\left(E_g\rho_g C_g+E_l\rho_l C_l\right)\frac{\partial T}{\partial t}+A\left(E_g\rho_g v_g C_g+E_l\rho_l v_l C_l\right)\frac{\partial T}{\partial x}+\frac{\partial}{\partial x}\left[Ap\left(E_g v_g+E_l v_l\right)\right]+\frac{1}{2}\frac{\partial}{\partial t}\left[A\left(E_g\rho_g v_g^2+E_l\rho_l v_l^2\right)\right]+\frac{1}{2}\frac{\partial}{\partial x}\left[A\left(E_g\rho_g v_g^3+E_l\rho_l v_l^3\right)\right]+q_g h_g \tag{6}$$

On the right side of the equation is the work done by fluid gravity, heat exchange energy, friction heat and inflow enthalpy. The enthalpy of inflow gas mainly exists in the bottom hole production interval, which can be expressed as (Livescu et al., 2010):

$$Q_{flux}=q_g h_e \tag{7}$$

Fluid friction heat is mainly caused by pipe wall shear force and is mainly affected by pipe wall roughness and flow velocity (Fu et al., 2022a; b). The friction heat generated by flow can be expressed by the following formula:

$$Q_{fric}=Af\frac{\rho_m v_m^2}{2D_h}v_m \tag{8}$$

During drilling, the flow of fluid in the wellbore will carry heat from the surrounding environment. We use the form developed by Hasan et al. (2002) to calculate the heat exchange energy in the wellbore.

$$Q_{in}=\frac{1}{A'}(T_{sr}-T)+\frac{1}{B'}(T_t-T) \tag{9}$$

$$A'=\frac{1}{2\pi}\left(\frac{k_e+r_{co}U_a T_D}{r_{co}U_a k_e}\right),\quad B'=\frac{1}{2\pi r_{ti}U_t} \tag{10}$$

where T_{sr} is the formation ambient temperature. The variation law of the ambient temperature and the compound heat transfer law between the wellbore and the formation can be referred to the article of Sun et al. (2019).

The annulus temperature field equation can be obtained by combining Eq. (4) and Eqs. (6)–(9):

$$A\left(E_g\rho_gC_g+E_l\rho_lC_l\right)\frac{\partial T}{\partial t}+A\left(E_g\rho_gv_gC_g+E_l\rho_lv_lC_l\right)\frac{\partial T}{\partial x}+\frac{\partial}{\partial x}\left[Ap\left(E_gv_g+E_lv_l\right)\right]+\frac{1}{2}\frac{\partial}{\partial t}\left[A\left(E_g\rho_gv_g^2+E_l\rho_lv_l^2\right)\right]+\frac{1}{2}\frac{\partial}{\partial x}\left[A\left(E_g\rho_gv_g^3+E_l\rho_lv_l^3\right)\right]+q_g\left(h_g-h_e\right)=-A\left(E_g\rho_gv_g+E_l\rho_lv_l\right)g\cos\theta+Af\frac{\rho_mv_m^2}{2D_h}v_m+\frac{1}{A'}\left(T_{sr}-T\right)+\frac{1}{B'}\left(T_t-T\right) \tag{11}$$

The temperature field equation of the fluid in the drill pipe is:

$$A_t\rho_lC_l\frac{\partial T_t}{\partial t}+A_t\rho_lv_lC_l\frac{\partial T_t}{\partial x}-\frac{\partial}{\partial x}\left(A_tpv_l\right)+\frac{1}{2}\frac{\partial}{\partial t}\left(A_t\rho_lv_l^2\right)+\frac{1}{2}\frac{\partial}{\partial x}\left(A_t\rho_lv_l^3\right)=-A_t\rho_lv_lg\cos\theta+A_tf\frac{\rho_lv_l^2}{2D_t}v_l-\frac{1}{B'}\left(T_t-T\right) \tag{12}$$

2.2. Supplementary submodels

2.2.1. Drift model relation

With the development of unconventional oil and gas resources, the number of complex well structures has increased sharply. The emergence of large-displacement horizontal wells and directional wells with well deviation angles of more than 90° poses a higher challenge to conventional wellbore multiphase flow theory. In a strongly unsteady wellbore multiphase flow system, the accuracy and stability of the drift flow models (1)–(3) depend on the constitutive Eq. (13) of the relative motion between phases (Zuber and Findlay, 1965). The applicability of the drift relation based on flow pattern division is reduced in miscellaneous well structures, resulting in high difficulty with the fine control of wellbore pressure. Therefore, it is necessary to establish a highly adaptive drift flow closure relation that can deal with complex well structures and complex flow conditions. Based on the idea of not dividing flow patterns and relying on the constructed multiphase flow experimental database, this paper analyzes the influence of various factors on the gas phase drift velocity and distribution law and establishes a drift relationship suitable for the full flow pattern domain and full dip range.

$$v_g=C_0\left(E_gv_g+E_lv_l\right)+v_{gm} \tag{13}$$

2.2.1.1. Multiphase flow experiment database. The drift relation without flow pattern division is developed based on experimental data and is highly dependent on the range of experimental data. Based on this, we built a database containing 3561 groups of gas–liquid two-phase flow experimental data from 30 different data sources. The specific information of the database is shown in Table 1. The experimental fluid types of the database include air water, air kerosene, air oil, air CMC solution, N_2-Luviskol and other fluid systems. The experimental liquid phase viscosity ranges from 0.001 to 6.8 Pa s; the inclination angle of the experimental pipe ranges from −90° to 90°, covering the flow types from gas–liquid co-flow to gas–liquid countercurrent; the hydraulic diameter of the pipeline ranges from 0.5 to 6 in, covering a wide range of flow space conditions. The experimental flow patterns include bubble flow, slug flow, agitated flow, and annular fog flow, which can cover all the flow patterns in the production process of oil and gas wells, drilling blowouts and the well-killing process. Liu et al. (2020) pointed out that the viscosity of fluid has a significant impact on the distribution of convection type, gas–liquid two-phase entrainment and the slug-mixing area. The viscosity of fluid varies widely in the process of drilling, well-killing and production. Therefore, the experimental data of high viscosity fluid are of great significance to reveal the field flow law.

Fig. 3 shows the distribution of experimental data in the database with experimental conditions. The diagrams along the diagonal axis of Fig. 3 are the vertical distribution diagrams of the database under the conditions of different apparent liquid velocity, apparent gas velocity, void fraction, hydraulic diameter, inclination angle, liquid viscosity and liquid density, showing the data distribution law of the database under a single factor. The scatter plots on both sides of the vertical distribution map are symmetrically distributed along the axis, respectively showing the data distribution under the combination of each of the above factors. It can concretely reflect the numerical range of data information in the database and the data distribution under different data combinations, so as to facilitate the selection of appropriate physical influencing factors when establishing the model. The red bar graph in Fig. 3 shows the distribution of data points under each influencing factor, the vertical coordinate indicates the amount of data points, and the blue line is the normal distribution pattern of data points. The scatter plot in Fig. 3 shows the distribution pattern of data under the interaction of each two factors, taking the second plot in the first row as an example, which characterizes the distribution of data points along the apparent liquid velocity at different apparent gas velocities. Thus, the scatter plot can show the mathematical pattern of the data under different physical factors.

According to the probability distribution of experimental data points in the figure, the apparent gas velocity distribution range of the database is 0–100 m/s; a large number of experimental data points are 0–20 m/s; the liquid phase apparent velocity distribution range is 0–8 m/s, and a large number of data points are 0–5 m. The void fraction data in the database are evenly distributed from low to high under the conditions of different pipe diameters, inclinations and viscosities, spanning all flow patterns in two-phase flow, and can characterize the influence of different factors on the gas–liquid two-phase distribution law. The liquid viscosity in the database ranges from 0.001 to 6.8 Pa s, but it is relatively concentrated in the range of 0.001–2.4 Pa s. In previous studies, research on the law of countercurrent flow is less relevant. The experimental data in the database in this paper are distributed in the range from −90° to 90°. Fig. 3 shows the distribution law under combinations of different factors. The two-phase flow data in the database are relatively evenly distributed under various influencing factors, and the data can reflect the influence law of various factors.

2.2.1.2. Drift relation construction. Before developing the mathematical forms of drift velocity and distribution coefficient, it is necessary to analyze the effects of different factors quantitatively and qualitatively based on the experimental database. The development of drift relations is mainly based on three ideas. The first is to establish the corresponding drift relation according to the drift characteristics and distribution characteristics of gas under different flow patterns based on the flow pattern characteristics in the pipeline; the second is the gas holdup correlation model, which establishes a unified relationship without dividing the flow pattern; the third is to develop the linear treatment of the discontinuity of the shunt drift relationship into the full flow unified relationship. Liu et al. (2020) summarized the existing

Table 1
Basic information of experimental database.

Data sources	Data quantity	Fluid type	Hydraulic diameter D_h, m	Angle, degree	Fluid viscosity, Pa s	Gas fraction
Godbole et al. (2011)	95	Air–water	0.127	−5–90	0.001	0.04–0.895
Gokcal (2008)	30	Air–high viscosity oil	0.0508	0	0.187–0.587	0.102–0.66
Soto-Cortes et al. (2019)	163	Air–mineral oil	0.0508	45–85	0.213	0.359–0.777
Vieira et al. (2015)	77	Air–water Air–CMC	0.076	90	0.001–0.01	0.688–0.979
Abdulkadir et al. (2010)	76	Silicone oil–air	0.067	90	0.0053	0.082–0.894
Ghiaasiaan et al. (1997)	210	Air–water Air–mineral oil Air–paraffinic oil	0.019	28–90	0.001–0.185	0.05–0.676
Das et al. (2002)	163	Air–water	0.0254	90	0.001	0.086–0.798
Abdul-Majeed (1996)	88	Air–kerosene	0.0508	0	0.0013–0.002	0.394–0.991
Minami and Brill (1987)	111	Air–water Air–kerosene	0.07793	0	0.001–0.002	0.549–0.994
Rosa et al. (2010)	73	Air–water	0.026	90	0.001	0.02–0.87
Schmidt et al. (2008)	71	N_2–water N_2–Luviskol	0.0545	90	0.001–6.88	0.08–0.96
Bhagwat and Ghajar (2012)	165	Air–water	0.0127	−90–90	0.001	0.06–0.9
França and Lahey (1992)	99	Air–water	0.019	0	0.001	0.063–0.944
Wang et al. (2016)	53	Air–water	0.057	90	0.001	0.072–0.907
Abdulkadir et al. (2016, 2010, 2020)	105	Air–silicone oil	0.067	0–90	0.00525	0.037–0.805
Liu et al. (2018)	120	Air–water	0.03	15–90	0.001	0.7–0.983
Mukherjee ane Brill, 1983	93	Air–kerosene Air–lubricating oil	0.038	−90–90	0.002–0.029	0.02–0.993
Skopich et al. (2015)	52	Air–water	0.0508	90	0.001	0.864–0.986
Caetano et al. (1992a, b)	161	Air–kerosene	0.034	90	0.001–0.0015	0.006–0.97
Chung et al. (2016)	18	Air–oil	0.0508	90	0.127–0.586	0.51–0.89
Sunthankar (2000)	173	Air–water	0.0887	15–90	0.001	0.086–0.807
Gokcal et al. (2006)	165	Air–oil	0.0508	0	0.181–0.257	0.08–0.5
Akor and Thesis (2013)	72	Air–water	0.0508	90	0.001	0.2–0.81
Mukherjee (1979)	465	Air–kerosene	0.0508	5–90	0.001	0.06–0.99
Magrini (2009)	140	Air–water	0.00762	0–90	0.001	0.976–0.998
Felizola (1992)	90	Air–kerosene	0.0051	0–90	0.00128–0.00167	0.108–0.561
Kouba (1986)	54	Air–water	0.0762	0	0.001	0.23–0.55
Hills (1976)	230	Air–water	0.150	90	0.001	0.054–0.492
Smith (2002)	105	Air–water	0.1016/0.1524	90	0.001	0.027–0.7144
Eghorieta et al. (2018)	44	Air–oil	0.0381	0	0.123–0.254	0.271–0.712

Note: [a] The entire data bank is available from the first author.

representative drift flow models related to these three voids and analyzed the relevant parameters in the model. The distribution coefficient model is a mathematical function of the void fraction, Reynolds number and phase density, and the drift velocity is a mathematical function of the pipe diameter, surface tension, inclination angle and void fraction. With the development of drift flow models, an increasing number of influencing factors have been considered. Based on the analysis of the physical structure and two-phase flow law of the developed model, on the basis of ensuring more comprehensive physical parameters and reducing the complexity of the model, the variable functions of distribution parameters and drift velocity can be expressed as Eqs. (14) and (15).

$$C_0 = f\left(\frac{\rho_g}{\rho_l}, \frac{\rho_l v_m D_h}{\mu_l}, \alpha, E_g\right) \tag{14}$$

$$v_{gm} = f\left(D_h, \rho_l, \rho_g, \mu_l, \sigma, \alpha, E_g\right) \tag{15}$$

Eq. (15) gives the physical factors affecting the drift velocity. Before establishing the drift velocity model, the influence law of each factor needs to be analyzed to determine the corresponding mathematical relationship. In view of the influence of various physical factors in multiphase flow, we summarize the following conclusions.

(1) The drift velocity is directly proportional to $\sqrt{gD_h}$. The coefficients under the conditions of vertical flow and horizontal flow are 0.35 and 0.45, respectively. The drift velocity at any angle can be constructed by the drift velocity of horizontal and vertical flow.
(2) Experiments show that the viscosity has a strong effect on gas slippage under different inclination angles, which is negatively correlated with gas drift velocity, but the current drift velocity formula is weakly correlated with viscosity.
(3) In gas–liquid two-phase flow, there is mutual interference among bubble groups, and the drift velocity of gas is different from that of a single bubble, which can be corrected by gas holdup.
(4) The drift velocity of gas shows a strong correlation with the pipe diameter (Lou et al., 2020; Liu et al., 2021), but the drift velocity of gas does not increase infinitely with increasing pipe diameter; that is, the influence of pipe wall-induced resistance will be limited, there is a critical diameter, and the bubble velocity is not affected by the pipe diameter after exceeding this diameter.

Based on the above analysis, we comprehensively consider the effects of the pipeline inclination angle, pipe diameter, fluid physical parameters and void fraction on the gas drift velocity and construct the prediction relationship of the drift velocity, which is given by Eq. (16).

$$v_{gm} = (0.35\sin\alpha + 0.45\cos\alpha) \times \sqrt{\frac{gD_h(\rho_l - \rho_g)}{\rho_l}}(1 - E_g)^{0.5} C_1 C_2 C_4 \tag{16}$$

where C_1 is the effect of liquid viscosity on gas drift velocity. Based

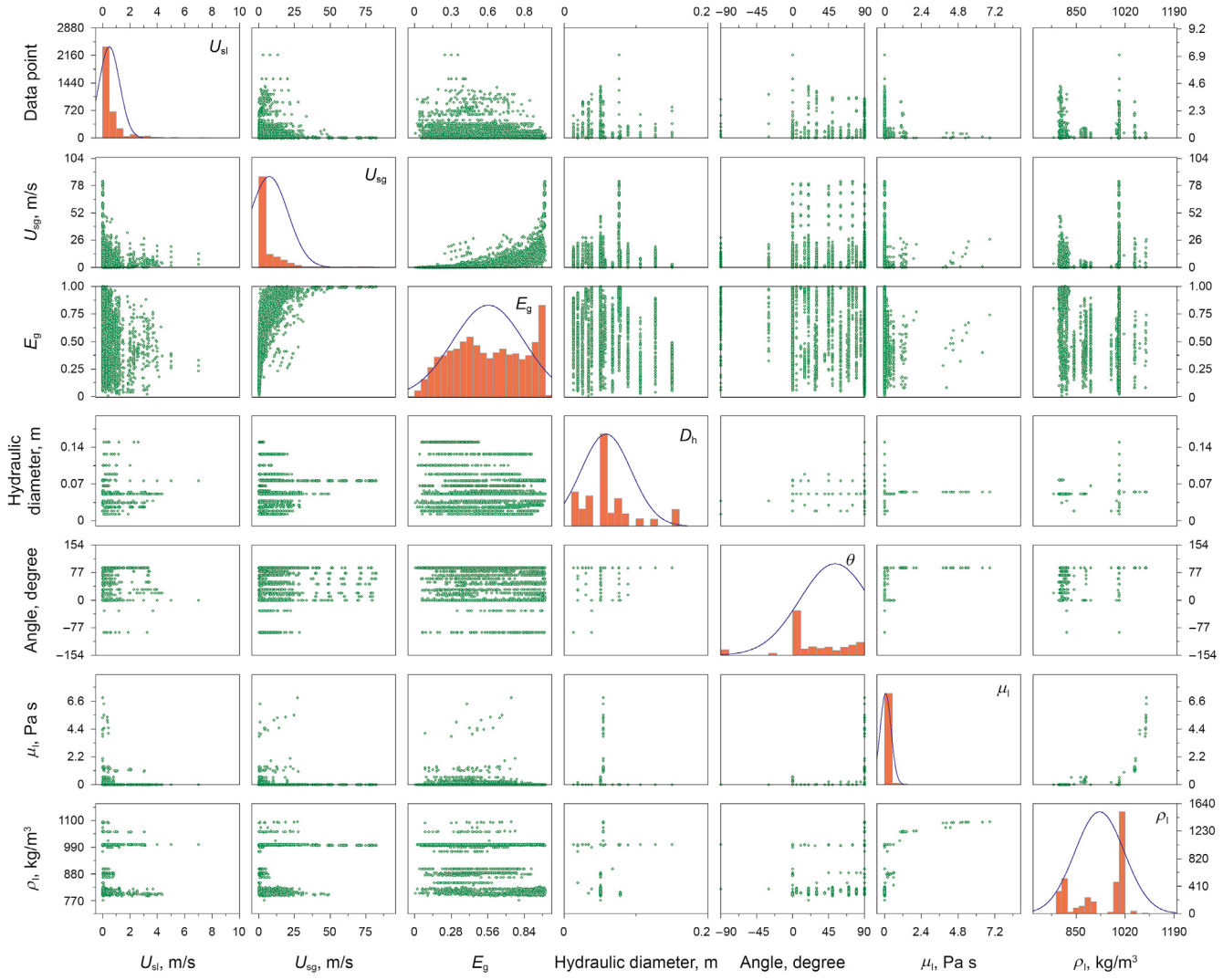

Fig. 3. Database parameter distribution.

on the analysis of existing experimental data, a logarithmic relationship of dimensionless viscosity is established. Eq. (17) characterizes the negative correlation between drift velocity and fluid viscosity.

$$C_1 = 1 - 0.036 \ln\left(\frac{\mu_l}{\mu_w}\right) \tag{17}$$

C_2 is the relevant parameter of the flow direction. According to the symbol reversal standard proposed by Bhagwat and Ghajar (2014) for downward flow, a continuous symbol switching function within the inclination angle $-50° < \alpha < 0°$ is constructed by using the idea of Fourier transform, and a symbol switching function satisfying $Fr < 0.1$ is constructed, such as Eq. (19). By combining the dip sign switching function with the Froude number switching function, a continuous function relationship satisfying the above two conditions is constructed, which is given by Eq. (18).

$$C_2 = 1 - \frac{2C_3}{1 + e^{50\sin(\alpha + 0.08)}} + \frac{2C_3}{1 + e^{50\sin(\alpha + 0.872)}} \tag{18}$$

$$C_3 = \begin{cases} \dfrac{1}{1 + e^{50\sin(Fr/0.1 - 1)}}, & Fr < 0.4 \\ 0, & Fr \geq 0.4 \end{cases} \tag{19}$$

C_4 is the relevant parameter of pipe diameter and liquid phase surface tension. The correction factor is defined by Eq. (20), which corrects the influence of pipe size parameters on gas drift velocity and meets the conditions of critical dimensionless pipe size.

$$C_4 = \begin{cases} \left(\dfrac{\sqrt{1/N_{Eö}}}{0.025}\right)^{0.15}, & N_{Eö} > 1600 \\ 1, & N_{Eö} \leq 1600 \end{cases} \tag{20}$$

Eq. (14) is the influencing factor of the distribution coefficient. Considering the influence of influencing factors on the distribution coefficient is the basis of establishing the model. For each influencing factor, we summarize the following conclusions.

(1) Fluid viscosity mainly affects the turbulence intensity of gas–liquid two-phase flow in the pipeline. When the

turbulent kinetic energy is low, the disturbance effect of fluid on the gas phase is small, the migration of gas in the pipeline is stable and tends to move toward the center of the pipeline under the action of lateral lift and the distribution of gas is uneven.

(2) The distribution coefficient is closely related to the flow pattern, so the distribution coefficient model should be a strong correlation function of gas holdup.

(3) The inclination angle of the pipeline changes the gravity system, affects the transformation boundary of the gas–liquid two-phase flow pattern and then affects the distribution coefficient.

Considering the influence of fluid viscosity, the classical mathematical form of the distribution coefficient without dividing the flow pattern is adopted. The distribution coefficient equation is composed of a low Reynolds number term and a high Reynolds number term. Combined with the analysis of Bhagwat and Ghajar (2014) on the influence of pipeline inclination, the YPL (yield-power-law) correlation form of gas content is introduced to construct the distribution coefficient equation, as shown in Eq. (21).

$$C_0 = \frac{a-\left(\rho_g/\rho_l\right)^2}{1+\left(Re_m/1000\right)^2} + \frac{1.2\left(\left(1+\left(\rho_g/\rho_l\right)^2\cos\alpha\right)/\left(1+\cos\alpha\right)\right)^{0.2\left(1-E_g\right)}+bE_g{}^c}{1+\left(1000/Re_m\right)^2} \tag{21}$$

In the distribution coefficient Eq. (21), a, b and c are constant coefficients, and parametric analysis needs to be carried out according to the data in the database. Data statistics involve the experimental data of many researchers. Due to the differences in experimental conditions and monitoring methods, the accuracy of experimental data is different, and there is a certain deviation in the experimental data under the condition of similar parameters. When using the experimental database for quantitative analysis, it is particularly important to ensure the accuracy of the experimental data. Before data fusion analysis, it is necessary to screen the effectiveness of the data. The existing models are used to verify the effectiveness of the statistical data. The models of Choi et al. (2012) and Liu et al. (2020) are selected to calculate all the data in the database to screen out the unreasonable experimental data in the database. After the screening, 3016 groups of experimental data remained. The parametric analysis of Eq. (21) is carried out using the screened multiphase flow experimental data. The minimum average error between the calculated gas holdup and the actual gas holdup is taken as the optimization objective for optimization analysis. Finally, the constant coefficients a, b and c after optimization are 2, −0.2, and 6.8, respectively.

2.2.2. Gas and liquid properties

2.2.2.1. Physical parameters of gas. Gas density has an important influence on the distribution law of gas–liquid two-phase flow and the propagation of pressure waves. The thermophysical parameters of gas are significantly affected by temperature and pressure. In this paper, PR EOS is used to calculate the gas density and heat capacity parameters (Peng and Robinson, 1976).

$$\left.\begin{aligned} &p = \frac{RT}{V-b} - \frac{a(T)}{V(V+b)+b(V-b)} \\ &Z^3-(1-B)Z^2+\left(A-3B^2-2B\right)Z-\left(AB-B^2-B^3\right)=0 \\ &A=\frac{ap}{R^2T^2},\quad B=\frac{bp}{RT},\quad Z=\frac{pV}{RT} \\ &a(T)=a(T_c)\alpha(T_r,\omega),\quad b(T)=b(T_c) \\ &a(T_c)=0.42724\frac{R^2T_c^2}{p_c},\quad b(T_c)=0.07780\frac{RT_c}{p_c} \\ &\alpha^{0.5}=1+\left(0.37464+1.54226\omega-0.26992\omega^2\right)\left(1-T_r^{0.5}\right) \end{aligned}\right\} \tag{22}$$

The viscosity of the gas is calculated using the model proposed by Lee et al. (1966).

$$\left.\begin{aligned} &\mu_g = 10^{-7}\frac{\left(16.919+36M_g\right)T^{1.5}}{T+64.506+5846.222M_g}\exp\left[X\left(\frac{\rho_g}{1000}\right)^{2.4-0.2X}\right] \\ &X = 0.01\left(350+\frac{30432.1}{T}+1000M_g\right) \end{aligned}\right\} \tag{23}$$

2.2.2.2. Physical parameters of drilling fluid. Considering the compressibility of drilling fluid along the well depth, we select the density model used in the drift flow simulation by Fjelde and Karlsen (2002), which is given by Eq. (24).

$$\rho_l = \rho_{l,0} + \frac{p-p_0}{c_l^2} \tag{24}$$

The viscosity of the drilling fluid is calculated by the model proposed by Zhao et al. (2008), which is given by Eq. (25).

$$f(p,T) = f(p_0,T_0)e^{A_\mu(T-T_0)+B_\mu(p-p_0)+C_\mu(T-T_0)(p-p_0)+D_\mu(T-T_0)^2} \tag{25}$$

3. Numerical scheme

For gas–liquid two-phase flow in the wellbore, many scholars use the implicit finite difference method. This method has strong applicability and high calculation efficiency in space and time discretization. As a mathematical method for solving nonlinear partial differential equations, finite difference has poor performance in flow conservation. Due to the accumulation of residual terms caused by iterative calculation, the convergence of the algorithm is impacted. When the gas reaches the wellhead, it expands rapidly, and the sudden change in gas holdup will put forward higher requirements for the convergence of the algorithm. In this paper, the finite volume method is used to establish the gas–liquid two-phase transient drift flow model and its solution method.

3.1. Scheme for drift flow model

3.1.1. Properties of the model

Partial differential equations are divided into three types: hyperbolic, parabolic and elliptic. Different types of equations describe different flow characteristics and physical backgrounds

and different mathematical properties, definite solution conditions and numerical algorithms. Before solving the multiphase flow equations, it is necessary to judge the relationship between the equation types and parameters to determine the definite solution conditions and numerical algorithms. The conservation Eqs. (1)–(3) of multiphase flow can be written into Eq. (26) in compact form.

$$\frac{\partial \boldsymbol{W}}{\partial t}+\frac{\partial \boldsymbol{F}}{\partial x}=\boldsymbol{S} \tag{26}$$

The compact form of conservation Eq. (27) can be quasilinear treated to facilitate the solution of eigenvalues and the determination of equation properties. Combined with the auxiliary equations, all physical parameters in the equations can be determined by the original variables $\boldsymbol{\Phi}(E_g,\ v_l,\ p)$. Using the chain rule, the original form of the quasilinear equation of the conservation equation can be expressed by Eq. (28).

$$\frac{\partial \boldsymbol{\Phi}}{\partial t}+\boldsymbol{J}_{\mathrm{W}}(\boldsymbol{\Phi})^{-1}\boldsymbol{J}_{\mathrm{F}}(\boldsymbol{\Phi})\frac{\partial \boldsymbol{\Phi}}{\partial x}=\boldsymbol{J}_{\mathrm{W}}(\boldsymbol{\Phi})^{-1}\boldsymbol{S} \tag{27}$$

The coefficient matrices in the formula are:

$$\boldsymbol{J}_{\mathrm{W}}(\boldsymbol{\Phi})=\begin{pmatrix} -\rho_l & 0 & \dfrac{E_l}{c_l^2} \\ \rho_g & 0 & \dfrac{E_g}{c_g^2} \\ \rho_g E_g\dfrac{C_0(v_g-v_l)}{1-C_0E_g} & \rho_l E_l+\rho_g E_g\dfrac{C_0E_g}{1-C_0E_g} & 0 \end{pmatrix}$$

$$\boldsymbol{J}_{\mathrm{F}}(\boldsymbol{\Phi})=\begin{pmatrix} -\rho_l v_l & \rho_l E_l & \dfrac{v_l E_l}{c_l^2} \\ \rho_g v_g+\rho_g E_g\dfrac{C_0(v_g-v_l)}{1-C_0E_g} & \rho_g E_g\dfrac{C_0E_g}{1-C_0E_g} & \dfrac{v_g E_g}{c_g^2} \\ \rho_g E_g v_g\dfrac{C_0(v_g-v_l)}{1-C_0E_g} & \rho_l E_l v_l+\rho_g E_g v_g\dfrac{C_0E_g}{1-C_0E_g} & 1 \end{pmatrix}$$

From the coefficient matrix of Eq. (27), it is impossible to directly solve the Jacobian matrix of the conservation equation. After a series of mathematical transformations, the characteristic root (28) of the Jacobian matrix can be obtained (Gryzlov, 2011); λ_1 and λ_3 represent the wave velocity of the pressure wave in the downstream and upstream directions, respectively, and λ_2 represents the propagation velocity of the gas volume wave. From the values of the three eigenvalues, it can be seen that the two-phase flow equation is a hyperbolic equation, which can be solved by the solution method of the linear convection equation.

$$\lambda_1=v_l-c_m,\quad \lambda_2=v_g,\quad \lambda_3=v_l+c_m \tag{28}$$

where c_m is the sound wave propagation velocity in the mixture, which is calculated by Eq. (29).

$$c_m=\sqrt{\frac{1}{\rho_m\left(\frac{E_g}{\rho_g c_g^2}+\frac{E_l}{\rho_l c_l^2}\right)}} \tag{29}$$

3.1.2. The AUSMV hybrid scheme

In terms of numerical solutions, the finite volume method (FVM) is widely used in computational fluid dynamics simulations because of its good conservation. Using the FVM of the staggered grid, we distribute the scalar parameters (the density, pressure and volume fraction of each phase) of multiphase flow at the center of the grid and the vector parameters (velocity of each phase) at the interface of the grid, as shown in Fig. 4. In the staggered grid system, the flow of the control volume will have a clear definition. Combined with the upwind scheme, the conservation equation can be discretized into Eq. (30).

$$\boldsymbol{W}_i^{n+1}=\boldsymbol{W}_i^n-\frac{\Delta t}{\Delta x}\left(\boldsymbol{F}_{i+1/2}^n-\boldsymbol{F}_{i-1/2}^n\right)+\Delta t\boldsymbol{S} \tag{30}$$

The methods for solving Eq. (30) can be divided into two categories: flux difference splitting FDS and flux vector splitting FVS. The FDS numerical scheme has a high discontinuous capture ability, but the processing process of the Jacobian matrix is cumbersome, and the solution efficiency is low. The FVS scheme has high efficiency, but it causes high numerical dissipation. The AUSM family algorithm combines the efficiency of FVS with the accuracy of FDS and introduces the characteristics of FDS into the FVS scheme to eliminate the excessive numerical loss of FVS. Due to its excellent performance of low dissipation and impact stability, the AUSM family algorithm is widely used in computational fluid dynamics. The advection upstream splitting model (AUSMV) combines the characteristics of the FVS and AUSM algorithms and has good stability and robustness. In this paper, the AUSMV scheme is used to solve the multiphase flow equation.

The flux vector $\boldsymbol{F}$ can be divided into a convection term and a pressure term. The convection term is composed of the flux of the gas phase and liquid phase. Based on this gas–liquid two-phase drift flow model, the inviscid flux vector can be described by Eq. (31).

$$\begin{aligned}\boldsymbol{F}_{i+1/2}&=\boldsymbol{F}_{\mathrm{l},i+1/2}^{\mathrm{c}}+\boldsymbol{F}_{\mathrm{g},i+1/2}^{\mathrm{c}}+\boldsymbol{F}_{i+1/2}^{\mathrm{p}}=\begin{pmatrix} E_l\rho_l v_l \\ 0 \\ E_l\rho_l v_l^2 \end{pmatrix}_{i+1/2} \\ &+\begin{pmatrix} 0 \\ E_g\rho_g v_g \\ E_g\rho_g v_g^2 \end{pmatrix}_{i+1/2}+\begin{pmatrix} 0 \\ 0 \\ p \end{pmatrix}_{i+1/2}\end{aligned} \tag{31}$$

In the above formula, the values of each parameter at the interface of the unit control body are given by Eq. (32).

$$\begin{cases} \boldsymbol{F}_{\mathrm{l},i+1/2}^{\mathrm{c}}=(E_l\rho_l)_{\mathrm{L}}\begin{pmatrix} 1 \\ 0 \\ v_l \end{pmatrix}_{\mathrm{L}}\tilde{V}_l^{+}+(E_l\rho_l)_{\mathrm{R}}\begin{pmatrix} 1 \\ 0 \\ v_l \end{pmatrix}_{\mathrm{R}}\tilde{V}_l^{-} \\ \boldsymbol{F}_{\mathrm{g},i+1/2}^{\mathrm{c}}=(E_g\rho_g)_{\mathrm{L}}\begin{pmatrix} 1 \\ 0 \\ v_g \end{pmatrix}_{\mathrm{L}}\tilde{V}_g^{+}+(E_g\rho_g)_{\mathrm{R}}\begin{pmatrix} 1 \\ 0 \\ v_g \end{pmatrix}_{\mathrm{R}}\tilde{V}_g^{-} \\ \boldsymbol{F}_{i+1/2}^{\mathrm{p}}=P^{+}\begin{pmatrix} 0 \\ 0 \\ p \end{pmatrix}_{\mathrm{L}}+P^{-}\begin{pmatrix} 0 \\ 0 \\ p \end{pmatrix}_{\mathrm{R}} \end{cases} \tag{32}$$

Velocity splitting and pressure splitting are given by Eqs. (33) and (34).

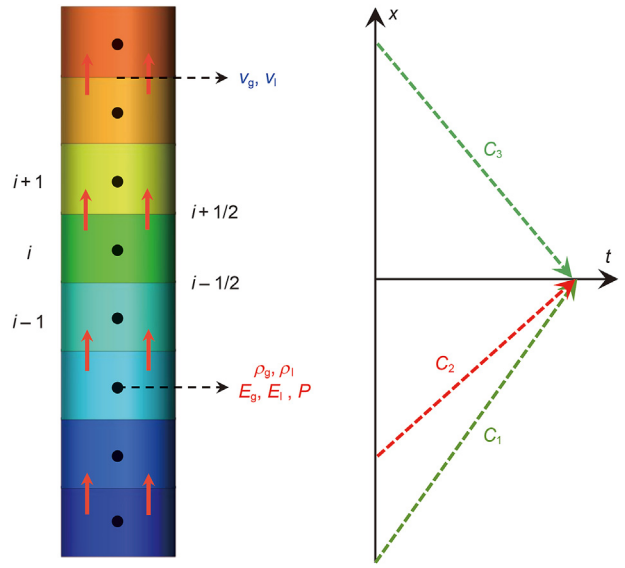

Fig. 4. Schematic diagram of staggered grid layout and characteristic line distribution.

$$\tilde{V}^{\pm}=\begin{cases}\chi V^{\pm}+(1-\chi)\dfrac{(v\pm|v|)}{2}, & |v|\le c\\ \dfrac{1}{2}(v\pm|v|), & |v|>c\end{cases},$$

$$V^{\pm}=\begin{cases}\pm\dfrac{(v\pm c)^2}{4c}, & |v|\le c\\ \dfrac{1}{2}(v\pm|v|), & |v|>c\end{cases} \tag{33}$$

$$P^{\pm}=V^{\pm}\begin{cases}\dfrac{1}{c}\left(\pm2-\dfrac{v}{c}\right), & |v|\le c\\ \dfrac{1}{v}, & |v|>c\end{cases} \tag{34}$$

The velocity vector at the center of each phase grid is used in the velocity splitting term, while the velocity in the pressure splitting term is the two-phase mixing velocity. The parameter calculation method in Eqs. (33) and (34) is given by Eq. (35).

$$c=\max(c_i,c_{i+1});\quad \chi_L=E_{g,R},\quad \chi_R=E_{g,L} \tag{35}$$

3.1.3. Numerical dispatch control

The AUSMV numerical scheme for the multiphase flow equation mentioned above has first-order accuracy. The central parameter values of the front and rear spatial grids are selected for parameter calculation, resulting in high numerical dissipation. Higher numerical dissipation will reduce the ability to capture the propagation velocity of the gas holdup wave, which also means that the time of gas reaching the wellhead after gas invasion and the prediction of gas holdup at the wellhead are not accurate. To improve the calculation accuracy, a smaller spatial step size must be selected, which will lead to a significant reduction in the calculation efficiency. Therefore, it is necessary to reconstruct the numerical scheme with high-order accuracy.

The high-order accuracy scheme of the time term includes the high-order prediction correction method and the Runge Kutta method. In this paper, the two-step Runge Kutta method is used to obtain the second-order accuracy of time.

$$\frac{d\boldsymbol{W}}{dt}=-\frac{\boldsymbol{F}(\boldsymbol{W})_{i+1/2}-\boldsymbol{F}(\boldsymbol{W})_{i-1/2}}{\Delta x}+\boldsymbol{S}(\boldsymbol{W})_i=\boldsymbol{L}(\boldsymbol{W})_i \tag{36}$$

$$\begin{cases}\boldsymbol{W}_i^{(1)}=\boldsymbol{W}_i^n+\Delta t\boldsymbol{L}(\boldsymbol{W})_i^n\\ \boldsymbol{W}_i^{n+1}=\dfrac{1}{2}\boldsymbol{W}_i^n+\dfrac{1}{2}\boldsymbol{W}_i^{(1)}+\dfrac{\Delta t}{2}\boldsymbol{L}(\boldsymbol{W})_i^{(1)}\end{cases} \tag{37}$$

If the numerical solution of the spatial difference scheme can maintain the properties of the exact solution, it needs to meet that the local maximum of the total variation does not increase and the local minimum does not decrease, which means that a high-order difference scheme needs to be constructed. All linear monotone-preserving schemes have only first-order accuracy, so it is necessary to construct a nonlinear policy-adjusted difference scheme. MUSCL technology (van Leer, 1979) can reconstruct the distribution of the original variables in the control body. Assuming that the distribution of the original variables in the control body is a primary or quadratic polynomial distribution, the parameters at the interface can be solved after the polynomial form is determined. However, the direct polynomial approximation will lead to the oscillation of the numerical solution. The slope limiter near the discontinuity can effectively solve this problem. In this paper, the original parameter $\boldsymbol{u}(v_l, v_g, E_g, E_l, \rho_l, \rho_g, p)$ is reconstructed by MUSCL technology and the van Albada slope limiter (Berger et al., 2005). The reconstructed interface parameters are introduced into the AUSMV algorithm, and then a numerical algorithm with second-order spatial accuracy is obtained.

$$\begin{cases}\boldsymbol{u}_{i+1/2}^{-}=\boldsymbol{u}_i+\dfrac{\phi_i}{4}[(1-k\phi_i)D_-\boldsymbol{u}_i+(1+k\phi_i)D_+\boldsymbol{u}_i]\\ \boldsymbol{u}_{i-1/2}^{+}=\boldsymbol{u}_i-\dfrac{\phi_i}{4}[(1-k\phi_i)D_+\boldsymbol{u}_i+(1+k\phi_i)D_-\boldsymbol{u}_i]\end{cases} \tag{38}$$

where ϕ_i is the van Albada slope limiter given by Eq. (39):

$$\phi_i=\frac{2D_+p_iD_-p_i+\varepsilon}{D_+p_i^2+D_-p_i^2+\varepsilon} \tag{39}$$

where ε is a small value (taken in this paper $\varepsilon=10^{-6}$) to prevent the denominator from being 0.

3.2. Scheme for energy conservation equations

In this study, the coupling solution of the multiphase flow equation and energy conservation equation is adopted. The specific coupling solution process can be seen in the calculation steps in Appendix A. For the energy equation, we use the forward difference in time and space, and the discrete format of the energy equation in the annulus is given by Eq. (40).

$$\begin{aligned}&\frac{A_i}{\Delta t}(E_g\rho_g C_g + E_l\rho_l C_l)^n_{i+1}\left(T^{n+1}_{i+1} - T^n_{i+1}\right) + \frac{A_i}{\Delta x}(E_g\rho_g v_g C_g + E_l\rho_l v_l C_l)^n_{i+1}(T^n_{i+1} - T^n_i) + \frac{1}{\Delta x}\left[A_{i+1}(pE_g v_g + pE_l v_l)^n_{i+1} - A_i(pE_g v_g + pE_l v_l)^n_i\right]\\&+\frac{A_{i+1}}{2\Delta t}\left[\left(E_g\rho_g v_g^2 + E_l\rho_l v_l^2\right)^{n+1}_{i+1}\right.\\&\left.-\left(E_g\rho_g v_g^2 + E_l\rho_l v_l^2\right)^n_{i+1}\right] + \frac{1}{2\Delta x}\left[A_{i+1}\left(E_g\rho_g v_g^3 + E_l\rho_l v_l^3\right)^n_{i+1} - A_i\left(E_g\rho_g v_g^3 + E_l\rho_l v_l^3\right)^n_i\right] + \left[\left(\frac{T}{A'}\right)^n_{i+1} + \left(\frac{T}{B'}\right)^n_{i+1}\right]\\&+g\cos\theta A_{i+1}(E_g\rho_g v_g + E_l\rho_l v_l)^n_{i+1} - \frac{A_{i+1}}{2D_{h,i}}\left(f\rho_m v_m^3\right)^n_{i+1} - \left(\frac{T_{sr}}{A'}\right)^n_{i+1} - \left(\frac{T_t}{B'}\right)^n_{i+1} + \left[q_g(h_g - h_e)\right]^n_{i+1} = 0\end{aligned} \tag{40}$$

The discrete format of the energy equation in the drill pipe is given by Eq. (41).

$$\begin{aligned}&\frac{A_{t,i+1}}{\Delta t}(\rho_l C_l)^n_{i+1}\left(T^{n+1}_{t,i+1} - T^n_{t,i+1}\right) + \frac{A_{t,i+1}(\rho_l C_l v_l)^n_{i+1}}{\Delta x}\left(T^n_{t,i+1} - T^n_{t,i}\right) + \frac{1}{\Delta x}\left[A_{t,i+1}(pv_l)^n_{i+1}\right.\\&\left.-A_{t,i}(pv_l)^n_i\right] + \frac{A_{t,i+1}}{2\Delta t}\left[\left(\rho_l v_l^2\right)^{n+1}_{i+1} - \left(\rho_l v_l^2\right)^n_{i+1}\right] + \frac{1}{2\Delta x}\left[A_{t,i+1}\left(\rho_l v_l^3\right)^n_{i+1} - A_{t,i}\left(\rho_l v_l^3\right)^n_i\right]\\&+g\cos\theta A_{t,i+1}(\rho_l v_l)^n_{i+1} - \frac{A_{t,i+1}}{2D_{h,i}}\left(f\rho_l v_l^3\right)^n_{i+1} + \frac{1}{B'^n_{i+1}}(T_t - T)^n_{i+1} = 0\end{aligned} \tag{41}$$

3.3. Boundary treatment

After the numerical scheme is discretized, the convective fluxes $\boldsymbol{F}_{1/2}$ and $\boldsymbol{F}_{N+1/2}$ on the boundary interface of the flow space have not been defined, so some method needs to be used to determine the values of the parameters of the boundary interface. Blowout, well-killing and pressure-controlled drilling are high-flow dynamic systems. There are strong disturbances in the pressure and gas content at the bottom and wellhead. Simple interpolation may reduce the accuracy or obtain a nonphysical understanding. Therefore, the conservation law of fluid needs to be considered for boundary condition flow. This problem can be solved based on the propagation characteristics of flow along the characteristic line. The characteristic line at the boundary is shown in Fig. 4. The equation properties of the drift flow model are discussed, and the propagation of gas volume waves and pressure waves are described.

Considering the hyperbolic characteristics of the equation, the multiphase flow equation can be transformed into a linear ordinary differential equation using the compatibility equation of the partial differential equation, and the compatibility relationship corresponding to the three characteristic roots can be expressed by Eq. (42) (Fjelde and Karlsen, 2002; Wang et al., 2020).

$$\begin{cases}C_1: \dfrac{\mathrm{d}}{\mathrm{d}t}p - \rho_l c_m(v_g - v_l)\dfrac{\mathrm{d}}{\mathrm{d}t}E_g - \rho_l E_l(v_g - \lambda_1)\dfrac{\mathrm{d}}{\mathrm{d}t}v_l = (v_g - \lambda_1)\left(f\dfrac{\rho_m v_m^2}{2D_h} + \rho_m g\cos\theta\right)\\ C_2: \dfrac{\mathrm{d}}{\mathrm{d}t}p + \rho_l c_m^2\dfrac{\mathrm{d}}{\mathrm{d}t}E_g = 0\\ C_3: \dfrac{\mathrm{d}}{\mathrm{d}t}p + \rho_l c_m(v_g - v_l)\dfrac{\mathrm{d}}{\mathrm{d}t}E_g - \rho_l E_l(v_g - \lambda_3)\dfrac{\mathrm{d}}{\mathrm{d}t}v_l = (v_g - \lambda_3)\left(f\dfrac{\rho_m v_m^2}{2D_h} + \rho_m g\cos\theta\right)\\ \dfrac{\mathrm{d}}{\mathrm{d}t} = \dfrac{\partial}{\partial t} + \lambda\dfrac{\partial}{\partial x}\end{cases} \tag{42}$$

Different flow conditions correspond to different flow boundaries. For overflow conditions during drilling, the bottom of the well is the mass flow inlet, and the wellhead is the pressure outlet. Taking the overflow condition as an example, we establish the boundary conditions of the bottom hole and wellhead.

Inlet boundary cell: The boundary of the bottom hole inlet is

the mass flow inlet. After drilling into the high-pressure formation, the formation fluid flows into the wellbore due to the differential pressure. The inflow mass flow can be predicted according to seepage theory. After the two-phase flow is known, the gas–liquid two-phase distribution can be calculated from the drift relationship, but the pressure at the bottom hole boundary is still unknown. The pressure can be solved by using the compatibility relationship corresponding to the propagation of the pressure wave in the upstream direction. The discrete format of compatibility equation C_1 is given by Eq. (43).

$$\begin{cases} \dfrac{p_{1/2}^{n}-p_{1/2}^{n-1}}{\Delta t}+(v_{\mathrm{l}}-c_{\mathrm{l}})_{1}^{n-1}\dfrac{p_{1}^{n-1}-p_{1/2}^{n-1}}{0.5\Delta x}-(\rho_{\mathrm{l}}c_{\mathrm{l}})_{1}^{n-1}\left[\dfrac{v_{\mathrm{l},1/2}^{n}-v_{\mathrm{l},1/2}^{n-1}}{\Delta t}+\dfrac{v_{\mathrm{l},1}^{n-1}-v_{\mathrm{l},1/2}^{n-1}}{0.5\Delta x}\right]=c_{\mathrm{l},1}^{n-1}\left(f\dfrac{\rho_{\mathrm{m}}v_{\mathrm{m}}^{2}}{2D_{\mathrm{h}}}+\rho_{\mathrm{m}}g\cos\theta\right)_{1}^{n-1},\ c_{\mathrm{m},1}^{n-1}>c_{\mathrm{l}} \\ \dfrac{p_{1/2}^{n}-p_{1/2}^{n-1}}{\Delta t}+\lambda_{1,1}^{n-1}\dfrac{p_{1}^{n-1}-p_{1/2}^{n-1}}{0.5\Delta x}-\left[\rho_{\mathrm{l}}c_{\mathrm{m}}(v_{\mathrm{g}}-v_{\mathrm{l}})\right]_{1}^{n-1}\left[\dfrac{E_{\mathrm{g},1/2}^{n}-E_{\mathrm{g},1/2}^{n-1}}{\Delta t}+\lambda_{1,1}^{n-1}\dfrac{E_{\mathrm{g},1}^{n-1}-E_{\mathrm{g},1/2}^{n-1}}{0.5\Delta x}\right]-\left[\rho_{\mathrm{l}}E_{\mathrm{l}}(v_{\mathrm{g}}-\lambda_{1})\right]_{1}^{n-1}\left[\dfrac{v_{\mathrm{l},1/2}^{n}-v_{\mathrm{l},1/2}^{n-1}}{\Delta t}\right. \\ \qquad\left.+\lambda_{1,1}^{n-1}\dfrac{v_{\mathrm{l},1}^{n-1}-v_{\mathrm{l},1/2}^{n-1}}{0.5\Delta x}\right]=(v_{\mathrm{g}}-\lambda_{1})_{1}^{n-1}\left(f\dfrac{\rho_{\mathrm{m}}v_{\mathrm{m}}^{2}}{2D_{\mathrm{h}}}+\rho_{\mathrm{m}}g\cos\theta\right)_{1}^{n-1},\ c_{\mathrm{m},1}^{n-1}\le c_{\mathrm{l}} \end{cases} \tag{43}$$

We find that there are unknown quantities $p_{1/2}^{n}$ and $E_{\mathrm{g},1/2}^{n}$ in discrete Eq. (43), and it is impossible to solve the two position quantities at the same time. Therefore, it is necessary to use the state equation of pressure and gas phase to establish the relationship between pressure and void fraction, form a closed equation containing only pressure and use the Newton Raphson iterative method for iterative solution.

Outlet boundary cell: The wellhead boundary is usually a known outlet pressure boundary. The density of each phase at the outlet can be determined by pressure. The unknown quantity is the velocity and volume fraction of each phase. The unknown quantity can be solved using the propagation characteristics of the volume wave and pressure wave downstream. The boundary parameters and flux can be solved by discrete compatibility equations C_2 and C_3.

When $c_{\mathrm{m},N}^{n-1}>c_{\mathrm{l}}$, there is no propagation of the volume wave. Through upwind discretization of the single-phase compatibility relationship corresponding to the C_3 wave, the liquid phase velocity is obtained:

$$\begin{aligned} &\frac{p_{N+1/2}^{n}-p_{N+1/2}^{n-1}}{\Delta t}+(v_{\mathrm{l}}+c_{\mathrm{l}})_{1}^{n-1}\frac{p_{N+1/2}^{n-1}-p_{N}^{n-1}}{0.5\Delta x} \\ &-(\rho_{\mathrm{l}}c_{\mathrm{l}})_{1}^{n-1}\left[\frac{v_{\mathrm{l},N+1/2}^{n}-v_{\mathrm{l},N+1/2}^{n-1}}{\Delta t}+\frac{v_{\mathrm{l},N+1/2}^{n-1}-v_{\mathrm{l},N}^{n-1}}{0.5\Delta x}\right] \\ &=c_{\mathrm{l},N}^{n-1}\left(f\frac{\rho_{\mathrm{m}}v_{\mathrm{m}}^{2}}{2D_{\mathrm{h}}}+\rho_{\mathrm{m}}g\cos\theta\right)_{N+1/2}^{n-1} \end{aligned} \tag{44}$$

When $c_{\mathrm{m},N}^{n-1}\le c_{\mathrm{l}}$, when the volume wave propagates to the wellhead, the compatibility relationship corresponding to the C_2 wave is discretized, and the equation containing only the gas volume fraction at the interface boundary can be obtained:

$$\begin{aligned} &\frac{p_{N+1/2}^{n}-p_{N+1/2}^{n-1}}{\Delta t}+\lambda_{2,N}^{n-1}\frac{p_{N+1/2}^{n-1}-p_{N}^{n-1}}{0.5\Delta x} \\ &-\left[\rho_{\mathrm{l}}c_{\mathrm{m}}\right]_{N}^{n-1}\left[\frac{E_{\mathrm{g},N+1/2}^{n}-E_{\mathrm{g},N+1/2}^{n-1}}{\Delta t}+\lambda_{2,N}^{n-1}\frac{E_{\mathrm{g},N+1/2}^{n-1}-E_{\mathrm{g},N}^{n-1}}{0.5\Delta x}\right]=0 \end{aligned} \tag{45}$$

When the volume wave propagates to the wellhead, the liquid phase velocity needs to be solved using the two-phase compatibility relationship of the C_3 wave, and the equation is discretized to obtain the liquid phase velocity:

$$\begin{aligned} &\frac{p_{N+1/2}^{n}-p_{N+1/2}^{n-1}}{\Delta t}+\lambda_{3,N}^{n-1}\frac{p_{N+1/2}^{n-1}-p_{N}^{n-1}}{0.5\Delta x}-\left[\rho_{\mathrm{l}}c_{\mathrm{m}}(v_{\mathrm{g}}-v_{\mathrm{l}})\right]_{N}^{n-1}\left[\frac{E_{\mathrm{g},N}^{n}-E_{\mathrm{g},N}^{n-1}}{\Delta t}\right. \\ &\left.+\lambda_{3,N}^{n-1}\frac{E_{\mathrm{g},N+1/2}^{n-1}-E_{\mathrm{g},N}^{n-1}}{0.5\Delta x}\right]-\left[\rho_{\mathrm{l}}E_{\mathrm{l}}(v_{\mathrm{g}}-\lambda_{3})\right]_{N}^{n-1}\left[\frac{v_{\mathrm{l},N+1/2}^{n}-v_{\mathrm{l},N+1/2}^{n-1}}{\Delta t}+\lambda_{3,N}^{n-1}\frac{v_{\mathrm{l},N+1/2}^{n-1}-v_{\mathrm{l},N}^{n-1}}{0.5\Delta x}\right] \\ &=(v_{\mathrm{g}}-\lambda_{3})_{N}^{n-1}\left(f\frac{\rho_{\mathrm{m}}v_{\mathrm{m}}^{2}}{2D_{\mathrm{h}}}+\rho_{\mathrm{m}}g\cos\theta\right)_{N}^{n-1} \end{aligned} \tag{46}$$

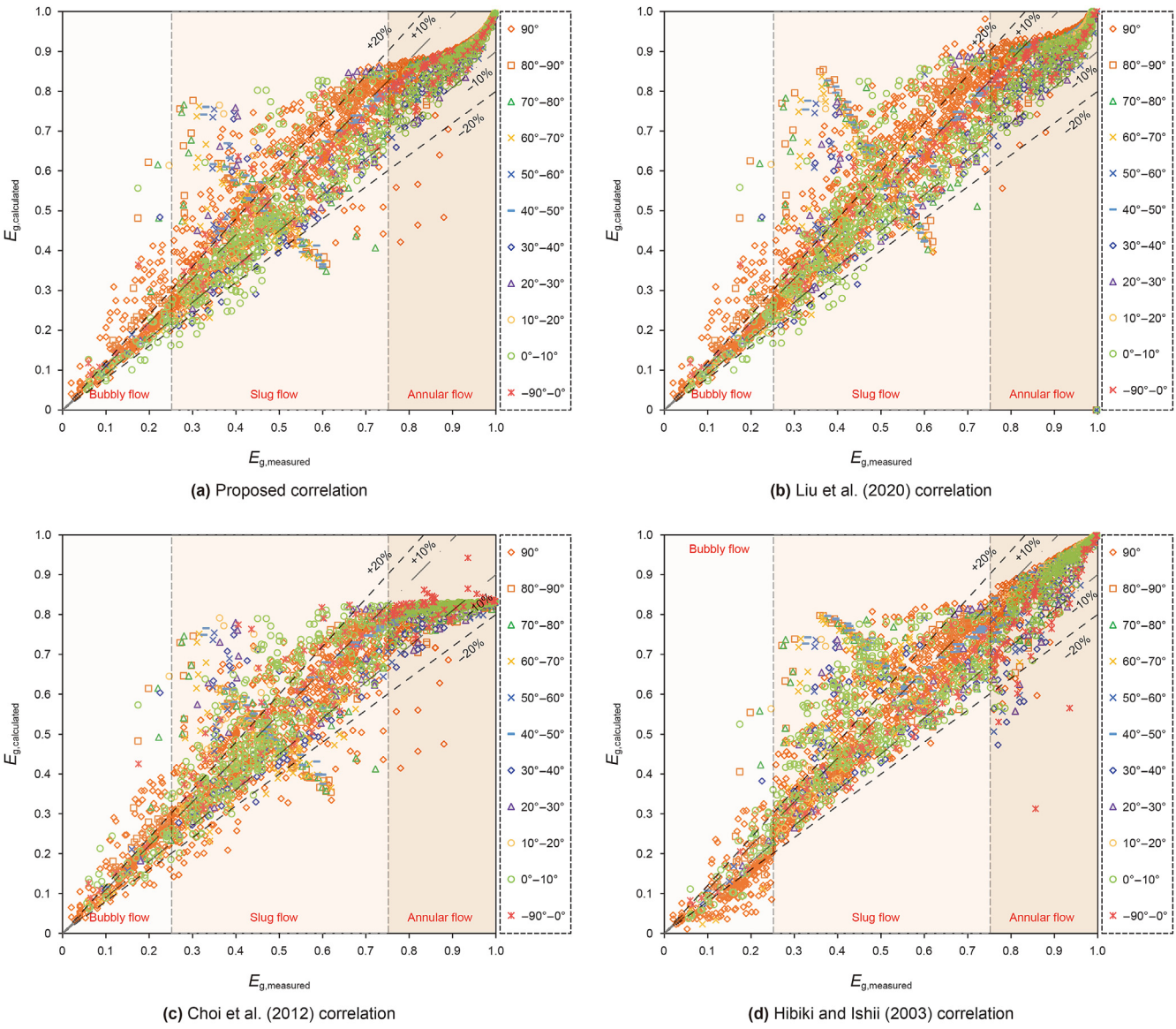

(a) Proposed correlation

(b) Liu et al. (2020) correlation

(c) Choi et al. (2012) correlation

(d) Hibiki and Ishii (2003) correlation

Fig. 5. Prediction results of gas holdup of different models.

Table 2
Comparison of model prediction results.

Statistical information		Present model	Liu et al. (2020)	Choi et al. (2012)	Hibiki and Ishii (2005)
±10%	B	52.63%	51.70%	31.89%	16.10%
	S	43.56%	38.50%	45.39%	45.33%
	A	95.26%	90.05%	43.89%	90.047%
±20%	B	65.94%	63.78%	60.99%	39.32%
	S	71.99%	64.19%	70.77%	68.64%
	A	99.24%	99.15%	99.05%	97.06%
±20%		80.86%	76.36%	80.00%	75.56%
±10%		62.63%	57.49%	43.56%	57.92%
Mean residual		0.0578	0.0691	0.0817	0.0662
Relative error		0.1329	0.1545	0.1640	0.1557
Standard deviation		0.0652	0.0833	0.0761	0.0839

Note: B represents bubbly flow; S represents slug flow, and A represents annular flow.

3.4. Convergence condition

The finite volume discretization in this study is expanded by the explicit scheme, so the stability and convergence of the equation are limited by the discretization conditions, and the time step is limited by the Courtant-Friedrichs-Lewy (CFL) conditions. The time step must be limited when simulating multiphase flow, and the limiting conditions are given by Eq. (47).

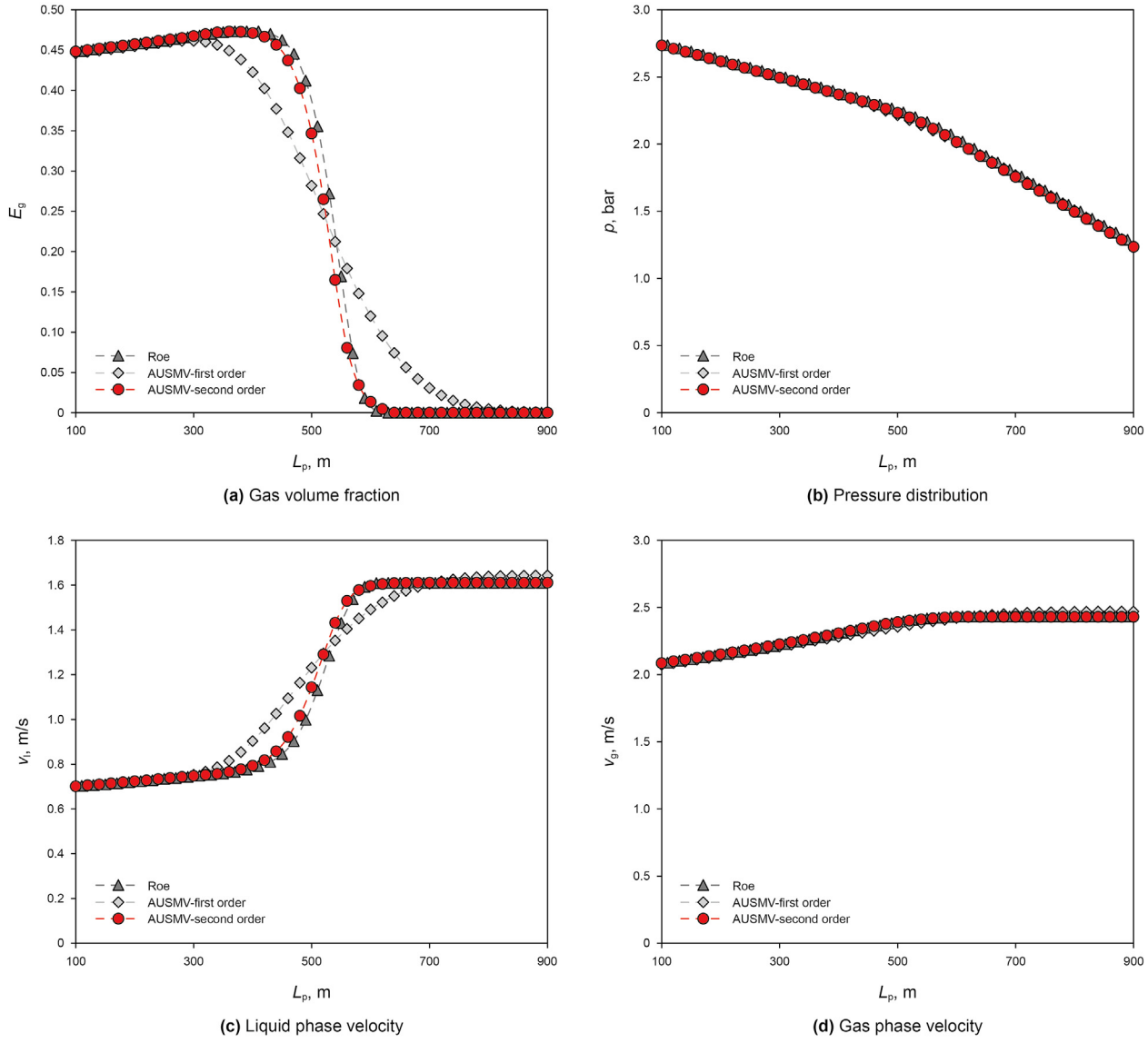

Fig. 6. Comparison of simulation results in the shock tube when $t = 250$ s.

Table 3
Basic parameters used in the simulation.

Parameters	Values	Parameters	Values
Annlus	244/224 mm	Specific heat capacity of drilling fluid	4200 J/(kg K)
Drillpipe	127/115 mm	Thermal conductivity of drilling fluid	0.72 W/(m K)
Drilling fluid rate	20 L/s	Thermal conductivity of casing/drillpipe	43.2 W/(m K)
Gas rate	1 kg/s	Thermal conductivity of cement	0.72 W/(m K)
Drilling fluid density	1000 kg/m^3	Thermal conductivity of gas	0.15 W/(m K)
Drilling fluid viscosity	0.05 Pa s	Thermal conductivity of formation	2.09 W/(m K)
Temperature gradient	0.0275 °C/m	Specific heat capacity of formation	999 J/(kg K)
Temperature gradient	25 °C	Density of formation	2090 kg/m^3

$$\Delta t \le \mathrm{CFL}\frac{\Delta x}{\max(|\lambda_1|,|\lambda_2|,|\lambda_3|)}, 0 < \mathrm{CFL} \le 1 \tag{47}$$

The time step is related not only to the value of the CFL but also to the propagation velocity of the pressure wave and volume wave. In this study, CFL is 0.5, and the propagation velocity of the three waves is the propagation velocity of the pressure wave in the liquid phase with the highest propagation velocity λ_3. In this paper, the approximate value is 1000 m/s.

4. Model validation and results analysis

4.1. Drift relation verification

The prediction accuracy of the drift relation is the key to ensuring multiphase flow simulation. Using the multiphase flow experimental database constructed in this paper, the drift relation (Eqs. (17) and (22)) and Liu model (Liu et al., 2020), Choi model (Choi et al., 2012), and Hibiki and Ishii model (Hibiki and Ishii,

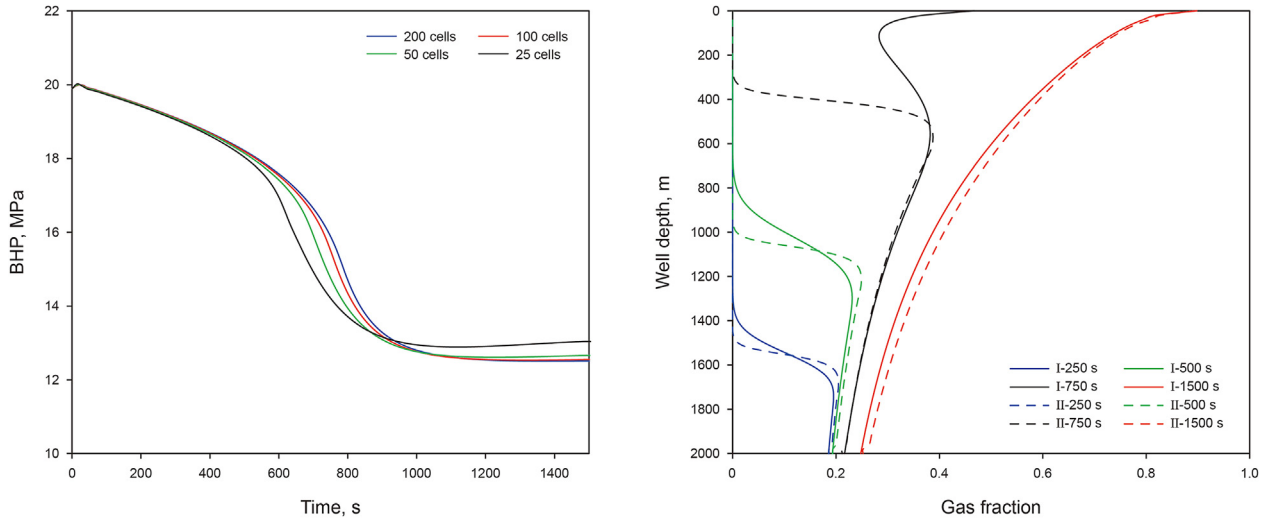

(a) Simulation results under different grid numbers

(b) Variation trend of wellbore gas content under 100 cells

Fig. 7. Numerical accuracy comparison.

2005) of this study are predicted and evaluated, and the prediction results are given in Fig. 5. The prediction of each model in Fig. 5 under different flow patterns is statistically analyzed, and the prediction accuracy within the error range of ±20% and ±10% is calculated. The specific parameters are given in Table 2. Combined with the results in Fig. 5 and Table 2, all models have the best prediction effect on the void fraction under the condition of annular fog flow, and the data points are centrally distributed within the error limit of ±20%. Under the experimental conditions, the predicted value of the distribution coefficient of the Choi model is close to 1.2, which deviates from the real distribution coefficient of annular fog flow. Therefore, the prediction effect is poor within the error range of ±10%, and the prediction accuracy is only 43.89%. The prediction accuracy of this model is the highest under the condition of annular fog flow, and the accurate prediction rates within the error limits of ±20% and ±10% reach 99.24% and 95.26%, respectively. In the drift relationship, the distribution coefficient at different flow rates is corrected by the value of the Reynolds number. The predicted value of the distribution coefficient at a low Reynolds number is low, resulting in the overall low prediction accuracy of bubble flow and slug flow. Under the condition of bubbly flow, the model in this paper performs best, and the accurate prediction rates of ±20% and ±10% error limits are 52.63% and 65.94%, respectively. Under slug flow conditions, the prediction accuracy of the Choi model and Hibiki and Ishii model is outstanding within the 10% error limit, and the prediction accuracy of this model is the best within the ±20% error limit.

To quantitatively analyze the overall prediction effect of the drift relationship, we analyze the prediction results of the four models by using the average residual error, average relative error and standard deviation. The specific parameters are given in Table 2. According to the data in the table, the prediction accuracy of this model within the ±20% error limit is 80.86%, and the prediction accuracy within the ±10% error limit is 62.63%, which is the most prominent among the four models. The average residual is used to

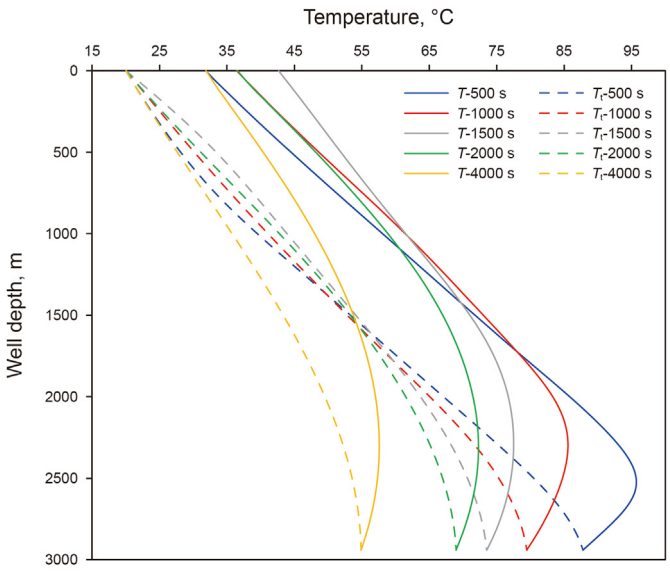

Fig. 8. Variation trend of temperature field in the wellbore.

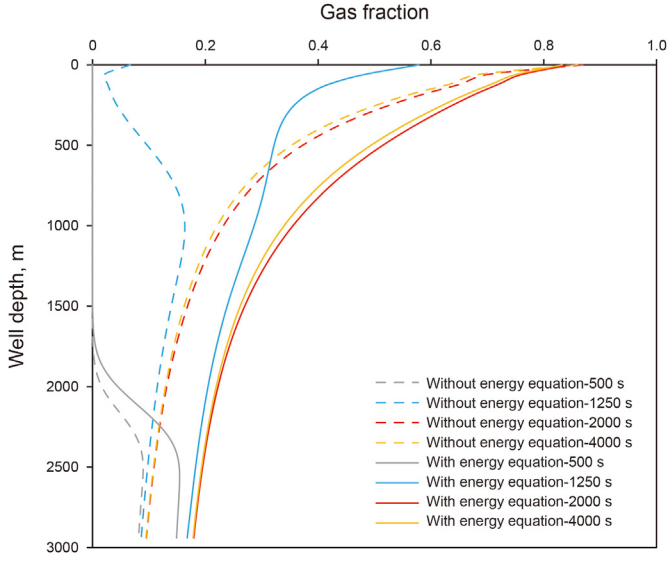

Fig. 9. Comparison of the calculation results of gas holdup in the wellbore with and without the energy equation.

represent the average value of the prediction error. Compared with other models, the average value of the prediction error of this model is the lowest, and the average deviation of the prediction results is the lowest. The standard deviation is used to characterize the uniformity of the prediction error distribution. The model in this paper has the lowest standard deviation, which shows that the prediction relative error of this model is relatively concentrated, and the value with a large prediction error is the least. Therefore, the model in this paper not only ensures the minimum prediction error but also has strong stability.

4.2. Numerical algorithm verification

The conventional AUSMV hybrid scheme has only first-order accuracy and low accuracy in discontinuous capture. After comparing the calculation results under different grid numbers, Udegbunam et al. (2015) pointed out that, to improve the calculation accuracy of the AUSMV hybrid scheme, the number of grids must be increased, which will lead to a longer algorithm convergence time and very slow simulation. Therefore, it is necessary to adopt a high-order accuracy algorithm to improve the calculation accuracy and efficiency.

We use the classical variable mass flow case proposed by Fjelde and Karlsen (2002) to verify the high-order accuracy algorithm with a limiter. At the initial moment, the pipeline is filled with static liquid. Within 10 s, the mass flow of liquid and gas increases from 0 to 3.0 and 0.02 kg/s, respectively, forming a gas volume fraction contact discontinuity and propagating from the inlet to the outlet. In this case, the distribution coefficient and drift velocity are 1.2 and 0.5, respectively. To ensure the effectiveness of the verification results, we continue to use this value in the calculation example. The simulation results using 50 spatial grids are shown in Fig. 6. The accuracy of the Roe scheme has been verified, and the fully numerical Roe solver is very accurate in solving the contact discontinuity problem. It can be seen from the calculation results in Fig. 6 that under the condition of the same number of spatial nodes, the numerical scheme of the first-order AUSMV has high numerical dissipation, the discontinuous capture ability of the volume wave is weak, and there are high errors in the prediction of gas position and phase velocity in the multiphase flow simulation. When using the second-order AUSMV numerical scheme with a limiter, the capture ability of gas volume waves is close to that of the Roe scheme, and the prediction accuracy of each phase velocity and pressure is also close to the numerical accurate solution.

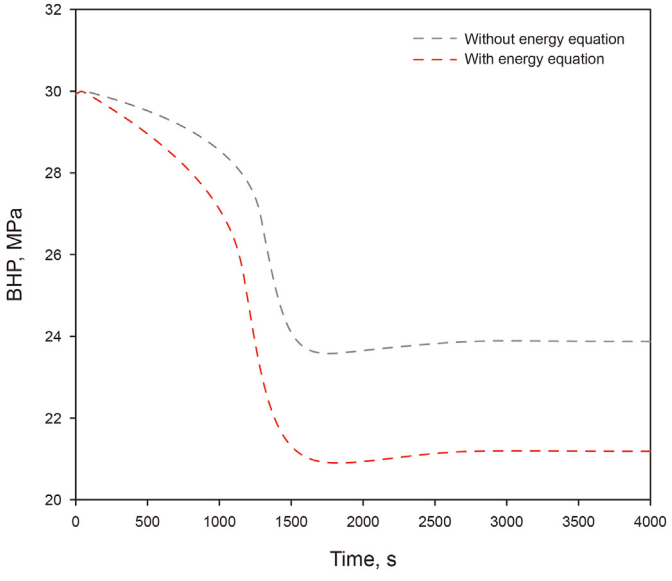

Fig. 10. Comparison of bottom hole pressure simulation results with and without the energy equation.

The numerical scheme with high-order accuracy is conducive to improving the identification of gas content distribution in the wellbore, and the prediction accuracy of gas migration and rising process is also relatively high. We discretize the well bore structure in Table 3 in different quantities. Fig. 7a shows the prediction results of bottom hole pressure with different cell numbers. From the results in the figure, it can be seen that the calculation accuracy of bottom hole pressure gradually improves with the increase of the number of grids. After more than 100 grids, the calculation accuracy of bottom hole pressure does not increase much. We discretize the well depth into 100 cells using the parameters in Table 3 and simulate the gas invasion process by using the numerical format of first-order accuracy and second-order accuracy. The change process of wellbore gas holdup is shown in Fig. 7b. In the early stage of gas invasion, due to the high bottom hole pressure, small gas expansion and low gas holdup in the wellbore, the prediction error of gas holdup by the first-order accuracy and second-order accuracy schemes is small. As the gas moves upward, the pressure decreases, resulting in the rapid expansion of the gas. At this time, the numerical dissipation generated by the calculation of void fraction is amplified. The closer to the wellhead, the greater the numerical dissipation of gas holdup and the lower the prediction accuracy of the gas front position. The results in the figure show that when the gas invasion takes 750 s, the second-order accuracy captures that the gas front reaches 300 m, while the first-order accuracy format simulation results show that the gas has reached the wellhead and has a high wellhead gas content. When the gas influx is stable, the wellbore gas holdup calculated by the first-order accuracy and second-order accuracy schemes is approximate. If the inflow performance does not change, the advantage of high-order accuracy will be reduced. The advantage of the high-order accuracy algorithm is reflected in the discontinuous capture ability. For the unsteady simulation of the gas invasion process, high-order accuracy can accurately predict the position of the gas front.

4.3. Comparison between models with and without the heat transfer effect

Udegbunam et al. (2015) pointed out that the AUSMV algorithm for wellbore multiphase flow uses an isothermal system for simulation calculation, which has a simple closed relationship and cannot truly reflect downhole conditions. Therefore, we used a 3000 m well to simulate the conventional AUSMV algorithm and the coupled energy equation AUSMV algorithm. The basic information of the well is consistent with that in Table 3. We set the initial temperature condition in the wellbore as the formation temperature and the injection temperature of the drilling fluid as 20 °C. Fig. 8 shows the temperature change curve in the wellbore during gas invasion. Since the initial condition is the formation temperature, with the injection of low-temperature drilling fluid, the high-temperature liquid in the drilling annulus is gradually replaced, and the temperature profile between the drill pipe and the annulus shows a decreasing trend. In the whole process, the wellhead temperature increases first and then decreases, mainly because the drilling fluid has a high specific heat capacity; cooling is not obvious in the whole flow process, and the downhole drilling fluid has a high temperature when flowing out. With the development of gas invasion, the gas gradually reaches the wellhead. Due to the low specific heat capacity of the gas, the temperature decreases significantly in the process of heat exchange and volume expansion, resulting in a decrease in the outlet temperature.

Table 4
Full scale blowout test parameters.

Parameter	Value	Parameter	Value
Casing inner diameter (0–1350 m)	330 mm	Gas molecular weight	28.02
Casing inner diameter (1350–2123 m)	224.5 mm	Drilling fluid viscosity	16 mPa s
Injection line outer diameter	88.9 mm	Drilling fluid density	1.168 g/cm^3
Depth of injection pipeline	1800 m	Pressure gauge location	1780 m

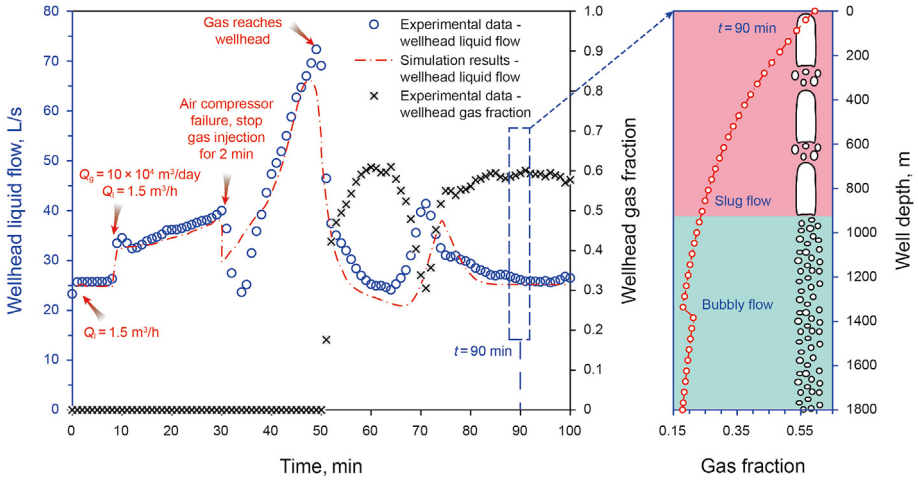

Fig. 11. Wellhead drilling fluid flow data during the gas injection blowout test of 10 × 10^4 m^3/day.

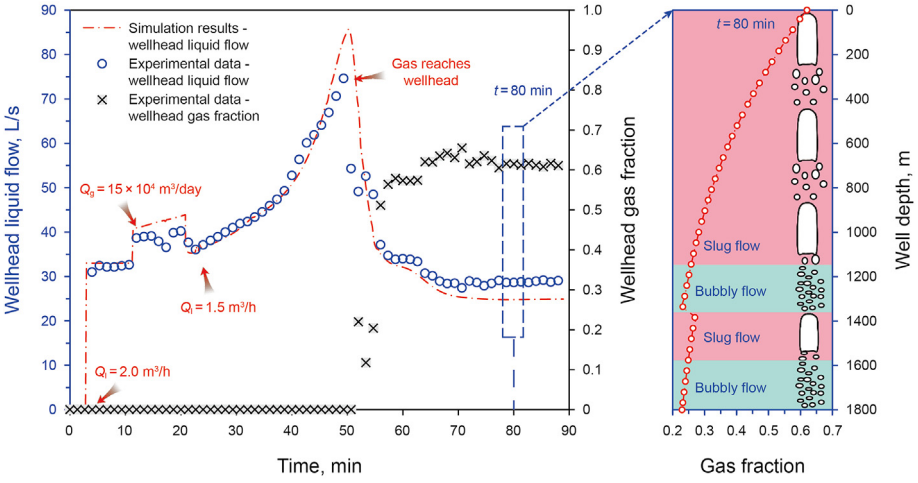

Fig. 12. Wellhead drilling fluid flow data during the gas injection blowout test of 15 × 10^4 m^3/day.

Fig. 9 shows the simulation results of gas invasion with and without considering the influence of the energy equation on the gas state. The numerical algorithm without considering the energy equation is the conventional AUSMV algorithm (Udegbunam et al., 2015; Eghorieta et al., 2018), and the gas state is predicted only by pressure. It can be seen from the results in the figure that the predicted difference in wellbore gas holdup gradually increases with increasing gas invasion time. When the gas invasion process tends to be stable, the maximum calculation error of gas holdup appears near the bottom hole, which is mainly caused by the large prediction error of the gas state caused by temperature and pressure conditions. Near the wellhead, because the prediction results of the gas state are similar, the prediction results of gas holdup are similar. Therefore, the coupled energy equation is very important for the accurate prediction of gas holdup in wellbores and the identification of gas–liquid two-phase flow patterns. Xu et al. (2018) noted that with increasing well depth, the temperature and pressure increased rapidly and gradually developed into high-temperature and high-pressure conditions. At this time, the prediction error of the gas state increased, and the energy equation became the key factor to improve the simulation accuracy of wellbore multiphase flow.

We show the influence of the above factors on the bottom hole pressure in Fig. 10. From the results in the figure, it can be found that the bottom hole pressure calculated by the multiphase flow algorithm considering the energy equation is lower than that without considering the energy equation, that the error value increases with the increase of gas influx, and that the difference from

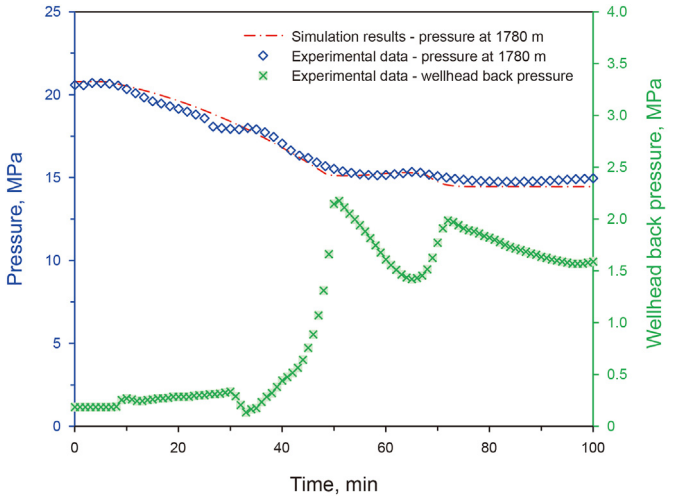

Fig. 13. Bottom hole pressure data during the 10 × 10^4 m^3/day gas injection blowout test.

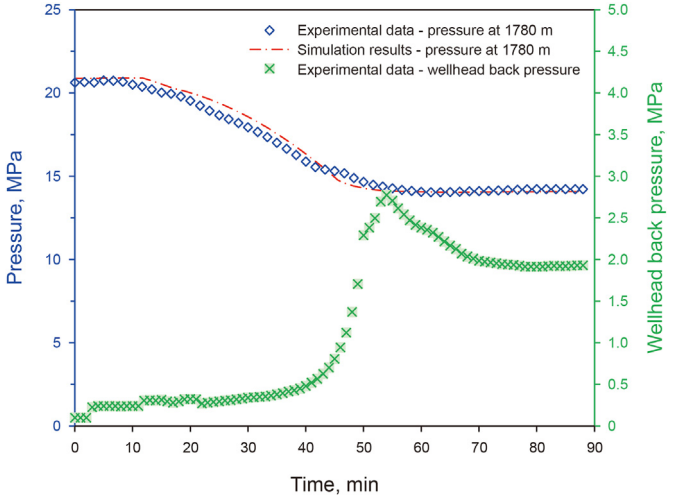

Fig. 14. Bottom hole pressure data during the 15 × 10^4 m^3/day gas injection blowout test.

the calculation results of bottom hole pressure at the time of gas influx stability is 2.69 MPa. This is mainly because the auxiliary equation for calculating the gas state by pressure overestimates the density of gas in the wellbore, resulting in the calculation result of gas holdup in the wellbore being too small, and then increases the difference of settlement results from two aspects. On the one hand, the gas density value is high, which leads to the large static pressure generated by the gas phase. On the other hand, under the condition of high gas density, the calculation result of gas phase velocity is small, and the gas content calculated by using the drift relationship is low. At this time, the static pressure generated by the drilling fluid increases, which eventually leads to a large difference in the bottom hole pressure. Under the conditions of high-yield gas well production or serious blowout, the calculation accuracy of bottom hole pressure plays an important role in production design and well-killing scheme formulation. The calculation accuracy of the conventional algorithm will restrict the formulation of the production scheme.

4.4. Gas kick experiment of full-scale experimental well

Relying on the experimental well, we carried out a full-scale blowout experiment. The gas–liquid phases of the experiment are air and mud. Air is injected into the blowout wellbore through the oil pipe through the series air compressor, and the drilling fluid is injected into the blowout wellbore simultaneously with air through the oil pipe through the back pressure pump to simulate the blowout process. An oil, gas and water three-phase flowmeter is installed at the wellhead to record the flow and gas holdup of the liquid phase of the well gas. The specific parameters of the experimental process are shown in Table 4.

The well structure and fluid injection parameters in the experimental process are used to simulate the blowout experimental process. Fig. 11 shows the comparison between the experimental monitoring value and simulation result of wellhead drilling fluid flow during blowout under the condition of gas production of 100000 m^3/day. The results in the figure show that the calculated results of the model in this paper are in good agreement with the experimental results. The simulation error of outlet flow when gas is seen at the wellhead is 9.7%, and the maximum error of the whole process is 25.4% (air compressor fault section). The simulation error is large in the 2 min period of air compressor failure, mainly because it takes a certain time for the on-site air compressor to inject gas into the bottom of the well. The numerical simulation adopts the switch of bottom hole gas production (shutdown for 2 min), which makes it difficult to accurately reproduce the starting process. Fig. 11 shows the distribution of wellbore gas content when the blowout is stable on the right. The simulation result of the wellhead gas content is 59.4%; the measured value is 58.8%, and the simulation error is 1.02%. Fig. 12 shows the comparison between wellhead measurement parameters and model calculation results during a 150000 m^3/day well blowout. The adjustment of blowout process parameters has little effect on multiphase flow; the simulation results are in good agreement with the experimental results, and the maximum simulation error is 12.1%. The right side of Fig. 12 shows the gas content in the wellbore under the blowout condition. The measured value of wellhead gas content is 61.2%; the simulation result is 62%, and the error is 1.3%.

Table 5
Basic parameters used in the simulation.

Parameter	Value	Parameter	Value
Well depth	5570 m	Drilling fluid density	1.28 g/cm^3
Casing shoe depth	3160 m	Yield point	13.28 Pa
Open hole size	220 mm	Consistency coefficient	0.44 Pa s^n
Drill pipe diameter	88/78 mm	power-law index	0.7
Casing diameter	244.5/224 mm (0–3160 m)	Yield point	30 L/s
Gas permeability	100 mD	Injection temperature	20 °C
Initial casing pressure	1 MPa	Injection temperature	25 °C
Geothermal gradient	0.0275 °C/m	Injection temperature	52 MPa
Building up section	870 m	Kickoff point depth	3200 m

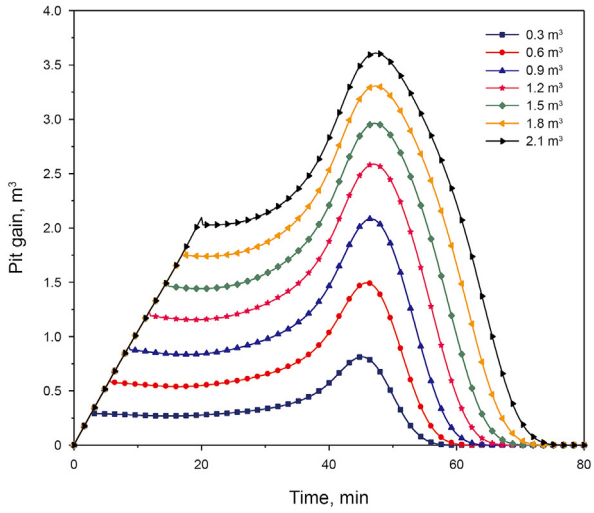

(a) Variation of mud pit increment under different gas invasion monitoring levels

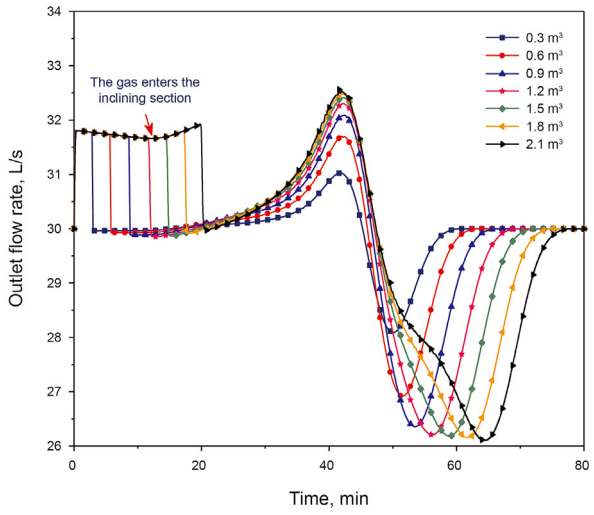

(b) Variation of wellhead flow under different gas influxes treated by MPD

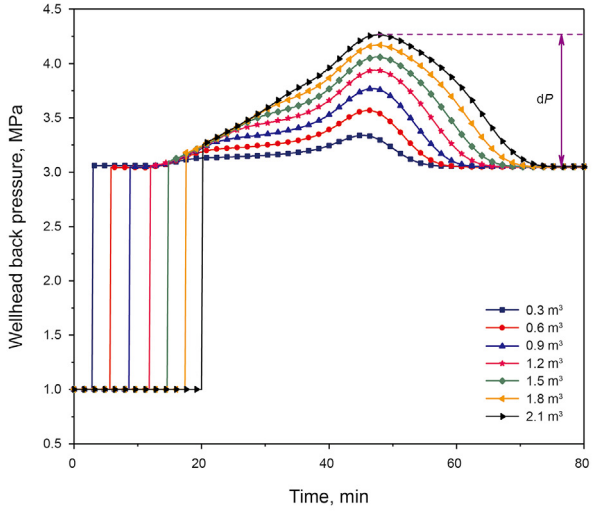

(c) Variation of wellhead back pressure under different gas influxes treated by MPD

Fig. 15. Wellhead response during MPD treatment of gas invasion.

Based on the simulation results of gas holdup in the wellbore, the distribution of the flow pattern in the wellbore can be deduced. The flow pattern distribution at the time of blowout stabilization is shown on the right of Figs. 11 and 12. The results in the figure show that, after the increase in gas injection, the bubble flow range in the wellbore is significantly reduced. Due to the influence of diameter change, bubbles and segments appear alternately in the wellbore. The flow pattern distribution has profound guiding significance for well-killing and production operation. The well-killing operation can adjust the well-killing strategy according to the flow pattern distribution in the wellbore, judge whether there is serious effusion in the wellbore during production operation and adjust the production strategy in time. Therefore, it is of great significance for oil and gas production to use this model to simulate wellbore flow, obtain gas holdup distribution and flow parameters and deduce wellbore flow pattern distribution based on the flow pattern division model.

A pressure gauge is installed at 1780 m underground to record the pressure change law during blowout. Figs. 13 and 14 show the comparison between the measured data of the pressure gauge and the calculation results of this model during 10×10^4 and 15×10^4 m^3/day blowouts, respectively. The simulation results are consistent with the law of field-measured values. The maximum calculation error of the model is 3.8% in the process of 10×10^4 m^3/day well blowout and 4.69% in the process of 15×10^4 m^3/day well blowout. The model calculation results have high accuracy.

4.5. Application in managed pressure drilling

MPD (managed pressure drilling) is an adaptive drilling process that is used to accurately control the pressure profile of the wellbore. Wellbore pressure is achieved by adjusting the overflow area of the wellhead throttling device, which can quickly change the wellhead back pressure. MPD has a certain gas invasion treatment capacity, reduces the operation process of well shut in and kill and can effectively improve drilling efficiency. However, the processing capacity of MPD is limited by the separation efficiency of the wellhead pressure-bearing device and gas–liquid separator. There are relatively few studies on this problem. The gas invasion processing process of MPD can be effectively analyzed by using the multiphase flow model in this paper, and the gas invasion processing capacity of MPD can be analyzed in combination with field equipment conditions. Liao et al. (2020) divided the MPD gas invasion treatment process into three stages: the stable gas invasion stage, the increased back pressure after gas invasion was detected, the suppression of the gas invasion process and the dynamic adjustment of the wellhead back pressure cycle exhaust process.

At present, there are relatively few studies of the treatment of gas invasion control of horizontal wells. We carried out the MPD gas invasion treatment process for a long horizontal well with a length of 1500 m. The specific parameters of the case well are given in Table 5. We carried out a detailed simulation of the gas treatment process under the conditions of different gas influxes. When the mud pit increment reaches the gas invasion monitoring level, it is necessary to immediately increase the wellhead back pressure to ensure the purpose of restraining the formation fluid invasion in a short time. Then, the bottom hole pressure is kept constant, and the wellhead pressure is dynamically adjusted to ensure that the gas in the wellbore stably circulates out of the wellbore and that there is no new gas intrusion at the bottom of the wellbore. Fig. 15 shows the variation laws of mud pit increment, wellhead flow and wellhead back pressure under different gas influxes treated by MPD.

Fig. 15a shows the variation law of mud pit increment in the whole process of MPD gas invasion and gas invasion treatment. When the mud pit increment reaches the gas invasion monitoring

level, the wellhead return air invasion is immediately increased, the mud pit liquid level increase is restrained, and the mud pit increment increases rapidly with the migration and expansion of gas. When the gas reaches the wellhead, the increment of the mud pit reaches the peak. With the circulating discharge of the gas, the liquid level of the mud pit gradually decreases until it returns to the initial state. It can be seen from the data in the figure that, with the decrease in the gas invasion monitoring level, the peak value of the mud pit increment gradually increases. The longer the gas invasion time, the greater the distribution length in the wellbore, the shorter the time for the mud pit increment to reach the peak value and the shorter the processing time.

Fig. 15b shows the variation trend of wellhead drilling fluid flow during MPD gas invasion treatment. It can be seen from the flow change of the mud pit in the figure that after the gas invasion of the horizontal well, the gas expands little in the horizontal section, and the change in bottom hole pressure is only caused by the change in friction. At this time, gas invasion is difficult to find. When the gas reaches the vertical well section, the gas begins to expand, the wellhead flow increases rapidly, the bottom hole pressure decreases, and the gas influx is easily found in the process of gas injection. When the wellhead pressure is increased after gas invasion is found, the gas in the wellbore is rapidly compressed. At this time, the drilling fluid flow at the wellhead suddenly decreases, mainly to ensure the conservation of volume in the wellbore. With the migration of gas to the wellhead, the wellhead drilling fluid flow increases gradually. When the mud pit increment reaches the peak, the outlet flow returns to the injection flow. With the discharge of gas, the outlet flow of the drilling fluid is gradually less than the inlet flow; the liquid level of the mud pit is gradually reduced until the gas is completely discharged from the wellbore, and the outlet flow returns to the inlet flow.

Fig. 15c shows the dynamic adjustment process of wellhead back pressure during gas circulation discharge. When workers find gas invasion, they quickly increase the wellhead pressure to restrain gas invasion. With gas migration to the wellhead, the gas volume expands, and the hydrostatic pressure in the wellbore decreases. It is necessary to increase the wellhead back pressure to compensate for the reduced pressure. When the gas content in the wellbore reaches the maximum value, the compensation value DP of the wellhead back pressure also develops to the maximum value. With the discharge of gas in the wellbore, the hydrostatic pressure gradually recovers, and the wellhead back pressure tends to be stable. The compensation value DP of wellhead pressure is closely related to the gas volume in the wellbore and positively related to the gas influx. The wellhead pressure in the process of pressure-controlled drilling mainly depends on the rotary control head to act on the annulus. The pressure bearing capacity of the rotary control head is limited, so the gas influx of the processor is also limited. In the future, our work will focus on considering the limited conditions of field equipment, analyzing the variation law of wellhead back pressure and the ability of MPD to deal with gas influx.

5. Conclusions

Considering the influence of temperature and pressure in wellbores on the gas–liquid two-phase transient flow process, a transient drift flow model coupling formation heat transfer and fluid energy change is developed in this paper. To improve the discontinuous capture ability of the multiphase flow model, a high-precision AUSMV numerical scheme is developed using MUSCL technology. Based on the constructed database, a drift closure relationship suitable for the full dip range in the full flow pattern domain is developed and introduced into the transient drift flow model. The developed transient model is used to analyze the influencing factors of multiphase flow calculation in the process of gas invasion. The main conclusions of this study are as follows:

(1) Based on data statistics, we have developed a database containing 3561 sets of experimental data of gas–liquid two-phase flow from 30 different data sources. Relying on the experimental database, we have developed a drift closure relationship suitable for the full dip range in the full flow pattern domain, which has good continuity. The problem of poor convergence of the multiphase flow algorithm caused by a discontinuous closed relationship is solved. Through model comparison, the prediction accuracy of this model within the ±20% error limit is 80.86%, and the prediction accuracy within the ±10% error limit is 62.63%, which is the most prominent among the four models. At the same time, the standard deviation of the model prediction error and the average residual of the model prediction are the smallest. The model prediction has strong stability while ensuring the minimum error.

(2) The AUSMV numerical scheme with second-order accuracy is constructed by using MUSCLinterface parameter reconstruction technology, the van Albada slope limiter and the two-step Runge Kutta method. The shock tube case shows that the second-order accuracy numerical scheme developed in this paper is equivalent to the discontinuous capture ability of the classical Roe method. The first-order algorithm produces high numerical dissipation and cannot accurately characterize the migration process of gas in the wellbore. The gas invasion process of a case well is compared and analyzed. The results show that the first-order accuracy numerical scheme leads to an inaccurate prediction of gas arrival time at the wellhead due to its high numerical dissipation, and the second-order accuracy scheme is conducive to accurate capture of the position of the gas front in the process of gas invasion.

(3) In this paper, the conventional AUSMV numerical algorithm is simulated and compared with the AUSMV algorithm coupled with the energy equation. The calculation of the gas state in the conventional algorithm only depends on the pressure, overestimates the gas density in the wellbore and underestimates the gas content, resulting in the high predicted value of wellbore pressure. Under the condition of the case well in this paper, the difference between the two algorithms for the estimated bottom hole pressure is 2.69 MPa, and this difference will increase with increasing well depth. Therefore, it is necessary to introduce the energy equation in the multiphase flow simulation of high-temperature and high-pressure wells.

(4) The algorithm is verified by the blowout experimental team of a full-scale test well. The blowout simulation results under the condition of gas injection of 10×10^4 m^3/day show that the simulation error of outlet flow when gas is seen at the wellhead is 9.7%, that the maximum error of the whole process is 25.4%, that the simulation error of wellhead gas holdup in the stable blowout stage is 1.02% and that the simulation error of bottom hole pressure is less than 3.8%. The blowout simulation results under the condition of 15×10^4 m^3/day gas injection show that the maximum

simulation error of wellhead gas holdup is 12.1%, that the simulation error of wellhead gas holdup in the stable blowout stage is 1.3% and that the simulation error of bottom hole pressure is less than 4.69%. The model calculation results have high accuracy.

(5) The model developed in this paper is used to analyze the pressure-controlled drilling process with high flow performance. The model developed in this paper can be used to simulate and analyze the whole process of MPD treatment of gas invasion. It can analyze whether the field equipment can deal with the current gas influx after overflow is found on site and then determine whether to convert to conventional well-killing.

Declaration of competing interest

We declare that we have no financial and personal relationships with other people or organizations that can inappropriately influence our work, there is no professional or other personal interest of any nature or kind in any product, service and/or company.

Acknowledgments

The work was supported by the National Natural Science Foundation of China (No. 51874045), National Natural Science Foundation–Youth Foundation (52104056), Department of Natural Resources of Guangdong Province (GDNRC[2021]56), Postdoctoral innovative talents support program in China (BX2021374), Scientific Research Program of Hubei Provincial Department of Education (T2021004).

Appendix A. Solution procedure

The solution flow of high-precision non-isothermal transient wellbore drift flow model is shown in Fig. A1.

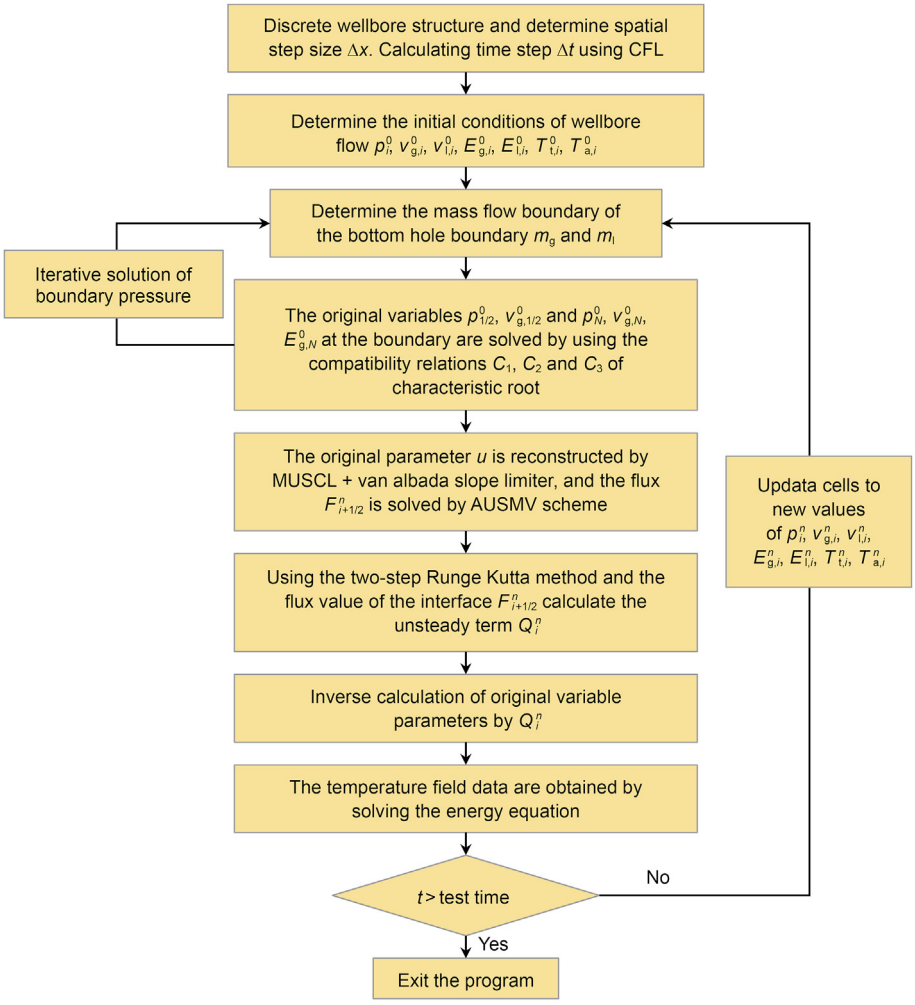

Fig. A1. Schematic of the solution procedure.

References

Abdulkadir, M., Hernandez-Perez, V., Lowndes, I.S., Azzopardi, B.J., Sam-Mbomah, E., 2016. Experimental study of the hydrodynamic behaviour of slug flow in a horizontal pipe. Chem. Eng. Sci. 156, 147–161. https://doi.org/10.1016/j.ces.2016.09.015.

Abdulkadir, M., Hernandez–Perez, V., Sharaf, S., Lowndes, I., Azzopardi, B., 2010. Experimental investigation of phase distributions of two-phase air-silicone oil flow in a vertical pipe. World Academy of Science, Engineering and Technology 61, 52–59.

Abdulkadir, M., Zhao, D., Abdulkareem, L.A., Asikolaye, N.O., Hernandez-Perez, V., 2020. Insights into the transition from plug to slug flow in a horizontal pipe: an experimental study. Chem. Eng. Res. Des. 163, 85–95. https://doi.org/10.1016/j.cherd.2020.08.025.

Abdul-Majeed, G.H., 1996. Liquid holdup in horizontal two-phase gas—liquid flow. J. Petrol. Sci. Eng. 15 (2–4), 271–280. https://doi.org/10.1016/0920-4105(95)00069-0.

Akor, I.C., 2013. Liquid Holdup in Vertical Air/Water Multiphase Flow with Surfactant. M.S. Thesis. University of Dayton, Dayton.

Ansari, A.M., Sylvester, N.D., Sarica, C., Shoham, O., Brill, J.P., 1994. A comprehensive mechanistic model for upward two-phase flow in wellbores. SPE Prod. Facil. 9 (2), 143–151. https://doi.org/10.2118/20630-PA.

Berger, M., Aftosmis, M., Muman, S., 2005. Analysis of slope limiters on irregular grids. In 43rd AIAA Aerospace Sciences Meeting and Exhibit 490. https://doi.org/10.2514/6.2005-490.

Bhagwat, S.M., Ghajar, A.J., 2012. Similarities and differences in the flow patterns and void fraction in vertical upward and downward two phase flow. Exp. Therm. Fluid Sci. 39, 213–227. https://doi.org/10.1016/j.expthermflusci.2012.01.026.

Bhagwat, S.M., Ghajar, A.J., 2014. A flow pattern independent drift flux model based void fraction correlation for a wide range of gas–liquid two phase flow. Int. J. Multiphas. Flow 59, 186–205. https://doi.org/10.1016/j.ijmultiphaseflow.2013.11.001.

Caetano, E.F., Shoham, O., Brill, J.P., 1992a. Upward vertical two-phase flow through an annulus—Part I: single-phase friction factor, Taylor bubble rise velocity, and flow pattern prediction. J. Energy Resour. Technol. 114 (1), 1–13. https://doi.org/10.1115/1.2905917.

Caetano, E.F., Shoham, O., Brill, J.P., 1992b. Upward vertical two-phase flow through an annulus—Part II: modeling bubble, slug, and annular flow. J. Energy Resour. Technol. 114 (1), 14–30. https://doi.org/10.1115/1.2905916.

Choi, J., Pereyra, E., Sarica, C., Park, C., Kang, J.M., 2012. An efficient drift-flux closure relationship to estimate liquid holdups of gas-liquid two-phase flow in pipes. Energies 5 (12), 5294–5306. https://doi.org/10.3390/en5125294.

Chung, S., Pereyra, E., Sarica, C., Soto, G., Alruhaimani, F., Kang, J., 2016. Effect of high oil viscosity on oil-gas flow behavior in vertical downward pipes. BHR Group, 10th North American Conference on Multiphase Technology.

Das, P.K., Das, G., Purohit, N.K., Mitra, A.K., 2002. Liquid holdup in concentric annuli during cocurrent gas-liquid upflow. Can. J. Chem. Eng. 80 (1), 153–157. https://doi.org/10.1002/cjce.5450800116.

Eghorieta, R.A., Afolabi, T.A., Panacharoensawad, E., 2018. Drift flux modeling of transient high-viscosity-liquid and gas two-phase flow in horizontal pipes. J. Petrol. Sci. Eng. 171, 605–617. https://doi.org/10.1016/j.petrol.2018.07.047.

Evje, S., Fjelde, K.K., 2002. Hybrid flux-splitting schemes for a two-phase flow model. J. Comput. Phys. 175 (2), 674–701. https://doi.org/10.1006/jcph.2001.6962.

Evje, S., Flåtten, T., 2003. Hybrid flux-splitting schemes for a common two-fluid model. J. Comput. Phys. 192 (1), 175–210. https://doi.org/10.1016/j.jcp.2003.07.001.

Felizola, H., 1992. Slug Flow in Extended Reach Directional Wells. University of Tulsa, Fluid Flow Projects.

Fjelde, K.K., Frøyen, J., Ghauri, A.A., 2016. A numerical study of gas kick migration velocities and uncertainty. SPE Bergen One Day Seminar. https://doi.org/10.2118/180053-MS.

Fjelde, K.K., Karlsen, K.H., 2002. High-resolution hybrid primitive–conservative upwind schemes for the drift flux model. Comput. Fluids 31, 335–367. https://doi.org/10.1016/S0045-7930(01)00041-X.

França, F., Lahey Jr., R.T., 1992. The use of drift-flux techniques for the analysis of horizontal two-phase flows. Int. J. Multiphas. Flow 18 (6), 787–801. https://doi.org/10.1016/0301-9322(92)90059-P.

Fu, W., Yu, J., Xiao, Y., Wang, C., Huang, B., Sun, B., 2022a. A pressure drop prediction model for hydrate slurry based on energy dissipation under turbulent flow condition. Fuel 311, 122188. https://doi.org/10.1016/j.fuel.2021.122188.

Fu, W., Yu, J., Xu, Y., Wang, C., Huang, B., Sun, B., 2022b. A pressure drop prediction model for hydrate slurry based on energy dissipation under laminar flow condition. SPE J. 1–11. https://doi.org/10.2118/209586-PA.

Ghiaasiaan, S.M., Wu, X., Sadowski, D.L., Abdel-Khalik, S.I., 1997. Hydrodynamic characteristics of counter-current two-phase flow in vertical and inclined channels: effects of liquid properties. Int. J. Multiphas. Flow 23 (6), 1063–1083. https://doi.org/10.1016/S0301-9322(97)00027-X.

Godbole, P.V., Tang, C.C., Ghajar, A.J., 2011. Comparison of void fraction correlations for different flow patterns in upward vertical two-phase flow. Heat Tran. Eng. 32 (10), 843–860. https://doi.org/10.1080/01457632.2011.548285.

Gokcal, B., 2008. An experimental and theoretical investigation of slug flow for high oil viscosity in horizontal pipes. ProQuest.

Gokcal, B., Wang, Q., Zhang, H.Q., Sarica, C., 2006. Effects of high oil viscosity on oil/gas flow behavior in horizontal pipes. SPE Annual Technical Conference and Exhibition. https://doi.org/10.2118/102727-MS.

Gryzlov, A.N., 2011. Model-based Estimation of Multi-phase Flows in Horizontal Wells. Ph.D. Dissertation. Delft Univ. Technol, Grad.

Han, P., Guo, L., 2015. Numerical simulation of terrain-induced severe slugging coupled by hydrodynamic slugs in a pipeline–riser system. Int. J. Heat Fluid Flow 56, 355–366. https://doi.org/10.1016/j.ijheatfluidflow.2015.10.005.

Hasan, A.R., Kabir, C.S., 2007. A simple model for annular two-phase flow in wellbores. SPE Prod. Oper. 22 (2), 168–175. https://doi.org/10.2118/95523-PA.

Hasan, A.R., Kabir, C.S., Sarica, C., 2002. Fluid Flow and Heat Transfer in Wellbores. Society of Petroleum Engineers, Richardson, Texas.

Hibiki, T., Ishii, M., 2005. Erratum: one-dimensional drift-flux model and constitutive equations for relative motion between phases in various two-phase flow regimes. Int. J. Heat Mass Tran. 48 (6), 1222–1223. https://doi.org/10.1016/j.ijheatmasstransfer.2004.12.001.

Hills, J.H., 1976. The operation of a bubble column at high throughputs: I. Gas holdup measurements. Chem. Eng. J. 12 (2), 89–99. https://doi.org/10.1016/0300-9467(76)87002-5.

Ishii, M., 1977. One-dimensional Drift-Flux Model and Constitutive Equations for Relative Motion between Phases in Various Two-phase Flow Regimes (No. ANL-77-47). Argonne National Lab, Ill. (USA). https://doi.org/10.2172/6871478.

Kouba, G.E., 1986. Horizontal Slug Flow Modeling and Metering. Ph. D. Dissertation. The University of Tulsa.

Lee, A.L., Gonzalez, M.H., Eakin, B.E., 1966. The viscosity of natural gases. J. Petrol. Technol. 18 (8), 997–1000. https://doi.org/10.2118/1340-PA.

Liao, Y., Sun, X., Sun, B., Wang, Z., Zhang, J., Lou, W., 2020. Wellhead backpressure control strategies and outflow response characteristics for gas kick during managed pressure drilling. J. Nat. Gas Sci. Eng. 75, 103164. https://doi.org/10.1016/j.jngse.2020.103164.

Liao, Y., Sun, X., Sun, B., Xu, J., Huang, D., Wang, Z., 2019. Coupled thermal model for geothermal exploitation via recycling of supercritical CO_2 in a fracture–wells system. Appl. Therm. Eng. 159, 113890. https://doi.org/10.1016/j.applthermaleng.2019.113890.

Liou, M.S., 1996. A sequel to AUSM: AUSM+. J. Comput. Phys. 129 (2), 364–382. https://doi.org/10.1006/jcph.1996.0256.

Liou, M.S., 2006. A sequel to AUSM, Part II: AUSM+-up for all speeds. J. Comput. Phys. 214 (1), 137–170. https://doi.org/10.1016/j.jcp.2005.09.020.

Liou, M.S., Steffen Jr., C.J., 1993. A new flux splitting scheme. J. Comput. Phys. 107 (1), 23–39. https://doi.org/10.1006/jcph.1993.1122.

Liu, Y., Luo, C., Zhang, L., Liu, Z., Xie, C., Wu, P., 2018. Experimental and modeling studies on the prediction of liquid loading onset in gas wells. J. Nat. Gas Sci. Eng. 57, 349–358. https://doi.org/10.1016/j.jngse.2018.07.023.

Liu, Y., Tong, T.A., Ozbayoglu, E., Yu, M., Upchurch, E., 2020. An improved drift-flux correlation for gas-liquid two-phase flow in horizontal and vertical upward inclined wells. J. Petrol. Sci. Eng. 195, 107881. https://doi.org/10.1016/j.petrol.2020.107881.

Liu, Y., Upchurch, E.R., Ozbayoglu, E.M., 2021. Experimental study of single Taylor bubble rising in stagnant and downward flowing non-Newtonian fluids in inclined pipes. Energies 14 (3), 578. https://doi.org/10.3390/en14030578.

Livescu, S., Durlofsky, L., Aziz, K., 2010. A semianalytical thermal multiphase wellbore-flow model for use in reservoir simulation. SPE J. 15 (3), 794–804. https://doi.org/10.2118/115796-PA.

Lou, W., Wang, Z., Li, P., Sun, X., Sun, B., Liu, Y., Sun, D., 2022. Wellbore drift flow relation suitable for full flow pattern domain and full dip range. Petrol. Explor. Dev. 49 (3), 694–706. https://doi.org/10.1016/S1876-3804(22)60058-2.

Lou, W., Wang, Z., Pan, S., Sun, B., Zhang, J., Chen, W., 2020. Prediction model and energy dissipation analysis of Taylor bubble rise velocity in yield stress fluid. Chem. Eng. J. 396, 125261. https://doi.org/10.1016/j.cej.2020.125261.

Magrini, K.L., 2009. Liquid Entrainment in Annular Gas-Liquid Flow in Inclined Pipes. Thesis. University of Tulsa.

Minami, K., Brill, J.P., 1987. Liquid holdup in wet-gas pipelines. SPE Prod. Eng. 2 (1), 36–44. https://doi.org/10.2118/14535-PA.

Mukherjee, H., 1979. An Experimental Study of Inclined Two-phase Flow. Thesis. The University of Tulsa.

Mukherjee, H., Brill, J.P., 1983. Liquid holdup correlations for inclined two-phase flow. J. Petrol. Technol. 35 (5), 1003–1008. https://doi.org/10.2118/10923-PA.

Nickens, H.V., 1987. A dynamic computer model of a kicking well. SPE Drill. Eng. 2 (2), 159–173. https://doi.org/10.2118/14183-PA.

Osher, S., Solomon, F., 1982. Upwind difference schemes for hyperbolic systems of conservation laws. Math. Comput. 38 (158), 339–374.

Peng, D.Y., Robinson, D.B., 1976. A new two- constant equation of state. Minerva Ginecol. 12 (11–12), 3069–3078. https://doi.org/10.1021/i160057a011.

Roe, P.L., 1981. Approximate Riemann solvers, parameter vectors, and difference schemes. J. Comput. Phys. 43 (2), 357–372. https://doi.org/10.1016/0021-9991(81)90128-5.

Rosa, E.S., Salgado, R.M., Ohishi, T., Mastelari, N., 2010. Performance comparison of artificial neural networks and expert systems applied to flow pattern identification in vertical ascendant gas–liquid flows. Int. J. Multiphas. Flow 36 (9), 738–754. https://doi.org/10.1016/j.ijmultiphaseflow.2010.05.001.

Schmidt, J., Giesbrecht, H., Van der Geld, C.W.M., 2008. Phase and velocity distributions in vertically upward high-viscosity two-phase flow. Int. J. Multiphas. Flow 34 (4), 363–374. https://doi.org/10.1016/j.ijmultiphaseflow.2007.10.013.

Shi, H., Holmes, J.A., Durlofsky, L.J., Aziz, K., Diaz, L., Alkaya, B., Oddie, G., 2005. Driftflux modeling of two-phase flow in wellbores. Soc. Pet. Eng 10, 24–33.

https://doi.org/10.2118/84228-PA.
Skopich, A., Pereyra, E., Sarica, C., Kelkar, M., 2015. Pipe-diameter effect on liquid loading in vertical gas wells. SPE Prod. Oper. 30 (2), 164–176. https://doi.org/10.2118/164477-PA.
Smith, T.R., 2002. Two-group Interfacial Area Transport Equation in Large Diameter Pipes. Ph.D. Thesis. Purdue University, West Lafayette, USA.
Soto-Cortes, G., Pereyra, E., Sarica, C., Rivera-Trejo, F., Torres, C., 2019. Effects of high oil viscosity on oil-gas upward flow behavior in deviated pipes. Exp. Therm. Fluid Sci. 109, 109896. https://doi.org/10.1016/j.expthermflusci.2019.109896.
Steger, J.L., Warming, R.F., 1981. Flux vector splitting of the inviscid gasdynamic equations with application to finite-difference methods. J. Comput. Phys. 40 (2), 263–293. https://doi.org/10.1016/0021-9991(81)90210-2.
Sun, X., Sun, B., Zhang, S., Wang, Z., Gao, Y., Li, H., 2018. A new pattern recognition model for gas kick diagnosis in deepwater drilling. J. Petrol. Sci. Eng. 167, 418–425. https://doi.org/10.1016/j.petrol.2018.04.035.
Sun, X., Wang, Z., Liao, Y., Sun, B., Gao, Y., 2019. Geothermal energy production utilizing a U-shaped well in combination with supercritical CO_2 circulation. Appl. Therm. Eng. 151, 523–535. https://doi.org/10.1016/j.applthermaleng.2019.02.048.
Sunthankar, A., 2000. Study of the Flow of Aerated Drilling Fluids in Annulus under Ambient Temperature and Pressure Conditions. M.S. Thesis. University of Tulsa, Tulsa, OK.
Sutton, I.S., 2013. Summarizing the deepwater horizon/macondo reports. Offshore Technology Conference. https://doi.org/10.4043/24027-MS.
Tang, H., Bailey, W., Stone, T., Killough, J., 2019. A unified gas-liquid drift-flux model for coupled wellbore-reservoir simulation. SPE Annual Technical Conference and Exhibition. https://doi.org/10.2118/195885-MS.
Udegbunam, J.E., Fjelde, K.K., Evje, S., Nygaard, G., 2015. On the advection-upstream-splitting-method hybrid scheme: a simple transient-flow model for managed-pressure-drilling and underbalanced-drilling applications. SPE Drill. Complet. 30 (2), 98–109. https://doi.org/10.2118/168960-PA.
van Leer, B., 1979. Towards the ultimate conservative difference scheme. V. A second-order sequel to Godunov's method. J. Comput. Phys. 32 (1), 101–136. https://doi.org/10.1016/0021-9991(79)90145-1.
Vieira, R.E., Parsi, M., Torres, C.F., McLaury, B.S., Shirazi, S.A., Schleicher, E., Hampel, U., 2015. Experimental characterization of vertical gas–liquid pipe flow for annular and liquid loading conditions using dual wire-mesh sensor. Exp. Therm. Fluid Sci. 64, 81–93. https://doi.org/10.1016/j.expthermflusci.2015.02.007.
Wang, C., Liu, G., Yang, Z., Li, J., Zhang, T., Jiang, H., Li, W., 2020. Downhole gas-kick transient simulation and detection with downhole dual-measurement points in water-based drilling fluid. J. Nat. Gas Sci. Eng. 84, 103678. https://doi.org/10.1016/j.jngse.2020.103678.
Wang, N., Sun, B., Gong, P., Wang, Z., 2017. Improved void fraction correlation for two-phase flow in large-diameter annuli. Chem. Eng. Technol. 40 (4), 745–754. https://doi.org/10.1002/ceat.201600119.
Wang, N., Sun, B., Wang, Z., Wang, J., Yang, C., 2016. Numerical simulation of two phase flow in wellbores by means of drift flux model and pressure based method. J. Nat. Gas Sci. Eng. 36, 811–823. https://doi.org/10.1016/j.jngse.2016.10.040.
Xu, Z., Song, X., Li, G., Wu, K., Pang, Z., Zhu, Z., 2018. Development of a transient non-isothermal two-phase flow model for gas kick simulation in HTHP deep well drilling. Appl. Therm. Eng. 141, 1055–1069. https://doi.org/10.1016/j.applthermaleng.2018.06.058.
Zhang, J., Wang, Z., Liu, S., Meng, W., Sun, B., Sun, J., Wang, J., 2020. A method for preventing hydrates from blocking flow during deep-water gas well testing. Petrol. Explor. Dev. 47 (6), 1354–1362. https://doi.org/10.1016/S1876-3804(20)60143-X.
Zhao, S.Y., Yan, J.N., Shu, Y., Zhang, H.X., 2008. Rheological properties of oil-based drilling fluids at high temperature and high pressure. J. Cent. S. Univ. Technol. 15 (1), 457–461. https://doi.org/10.1007/s11771-008-0399-7.
Zuber, N., Findlay, J.A., 1965. Average volumetric concentration in two-phase flow systems. J. Heat Tran. 87 (4), 453–468. https://doi.org/10.1115/1.3689137.